MECHANICAL CHARACTERIZATION AND MODELING OF COMPOSITE MATERIALS DURING COMPRESSION AND ACTUATION

by

Xuemin Wang

APPROVED BY SUPERVISORY COMMITTEE:

____
Hongbing Lu, Chair

____
Ray H. Baughman

____
Dong Qian

____
Majid Minary-Jolandan

This PhD dissertation

is dedicated to my family.

MECHANICAL CHARACTERIZATION AND MODELING OF COMPOSITE MATERIALS DURING COMPRESSION AND ACTUATION

by

XUEMIN WANG, BS, MS

DISSERTATION

Presented to the Faculty of

The University of Texas at Dallas

in Partial Fulfillment

of the Requirements

for the Degree of

DOCTOR OF PHILOSOPHY IN

MECHANICAL ENGINEERING

THE UNIVERSITY OF TEXAS AT DALLAS

August 2018

ACKNOWLEDGMENTS

First and foremost I would like to express my sincere gratitude to Dr. Hongbing Lu, a role model and mentor, for his training and guiding me patiently during my four years at The University of Texas at Dallas. Dr. Lu not only gave me tremendous academic support, but also gave me many excellent opportunities. Without Dr. Lu's persistent help, this dissertation would have not been possible.

I also want to give my special appreciation to my dissertation committee members, Dr. Ray H. Baughman, Dr. Dong Qian, and Dr. Majid Minary-Jolandan, for their encouragement and insightful comments. I would like to thank Dr. Baughman and Dr. Qian's guidance for the collaborating work and to help me on Chapter 3 writing. I would like to thank Dr. Minary to give me access to his laboratory and research equipment.

I would like to thank my collaborators, Dr. Monica Jung De Andrade, Dr. Jiuke Mu and Mr. Jiacheng Huang. I would like to thank Dr. Jung De and Mr. Huang for their help on SEM and sample preparation. I would like to thank Dr. Mu for his help on experiments for validation of the polymer-run muscles theory. Also, I would like to thank my colleagues in the Mechanics of Advanced Materials Lab. In particular, I would like to thank Dr. Huiyang Luo and Dr. Zhenxing Hu for their suggestions for designing experiments and writing journal articles. I would like to thank Dr. Yingjie Du and Dr. Tingge Xu, who are the former PhD students of Dr. Lu, for sharing their nanoindentation experience with me and giving me suggestions about research. I would also like to thank Mr. Rui Zhang for his suggestions on finite element simulations.

Last, but not the least, I would like to thank my parents-in-law, my parents and my sister for their unconditional support and love. I would also like to thank my beloved husband, Lianjun Wu and my son, Ethan Wu, for giving me such a good family, and for always cheering me up.

I also acknowledge the funding support from the National Science Foundation (Grant # CMMI-1636306, CMMI-1661246, and FAIN-1726435).

June 2018

MECHANICAL CHARACTERIZATION AND MODELING
OF COMPOSITE MATERIALS DURING COMPRESSION AND ACTUATION

Xuemin Wang, PhD
The University of Texas at Dallas, 2018

Supervising Professor: Hongbing Lu, Chair

Composites have a wide range of applications due to their excellent mechanical properties. In order to investigate the mechanisms of the recently developed composites, it is critical to characterize and model the performance of such composites for load-bearing applications. The high tensile strength of polymer matrix composites is mainly derived from the high strength of the carbon fibers embedded in the matrix. Fibers typically have high strength in tension. However, their compressive strengths are generally much lower than tensile strengths due to weak fiber/matrix interfacial shear strength. A new approach was recently developed to overwrap an individual carbon fiber with carbon nanotube (CNT) sheet, which is subsequently impregnated into a polymer matrix to enhance the interfacial shear strength and therefore increase the compressive strength without degrading the tensile properties of the carbon fibers. A theoretical model is established to identify the appropriate thickness of the interphase region formed by CNTs embedded in matrix. Fibers are modeled as an anisotropic elastic material, and the interphase region and matrix are considered as isotropic. A micro-buckling problem is considered to take into account of the unidirectional composite under elastic micro-buckling. The formulated problem is solved numerically and the results are compared with finite element simulations for verification. It is determined that the critical load at the onset of buckling is lower in an anisotropic carbon fiber composite than

in an otherwise isotropic composites due to lower transverse properties in anisotropic fibers. An optimal thickness for the CNT and matrix is determined and this finding will provide a guidance in the manufacture of composites using aligned CNTs as fillers in the interphase region.

The other type of composite is made of CNT yarn and polymer, which can be used as artificial muscles. The topology of this type of artificial muscle is polymer coated on a twisted or coiled CNT core, which can provide higher performance than the muscles made of guest-filled, twisted and coiled CNT yarns. However, the mechanisms of torsion and tension of the two artificial muscles are unclear. A theoretical model considering the torque balance between the polymer and yarn, both before and after twisting actuation is established to predict the torsional stroke. The theory captures the two primary mechanistic contributions to the torsional actuation of a polymer coated CNT yarn artificial muscle, where both polymer swelling and softening combine to partially release elastically stored torsional energy in the core yarn. This theory shows that while a low polymer thickness to core diameter ratio limits the capability of the polymer to compress the core and maintain the initially inserted twist before actuation, a very high polymer thickness to core diameter ratio provides less release of such inserted twist after the polymer coated CNT yarns is actuated. Consequently, there is an optimum polymer thickness to core diameter ratio that maximizes torsional stroke. We next theoretically predict the stress dependence of tensile stroke and contractile work capacity for coiled polymer coated CNT yarns and polymer infiltrated CNT yarns for isobaric actuation.

Another theoretical model established is for nylon artificial muscle. The torsional nylon artificial muscle is fabricated by twisting nylon wire into coil spring. When subjected to temperature fluctuations, nylon muscle fiber can sustain 300 000 heating-cooling cycles rotation to spin a magnet rotor in three phase coil. In this process, the rotor's mechanical energy transfers to electrical energy. The theoretical model captures the entire process by considering all the torques acted on the magnet, hence temperature, electrical field will be incorporated. Transfer efficiency and parameters effect on kinetic energy are studied. Numerical results show that the kinetic energy increases with the artificial muscle diameter, which is consistent with experimental observation. Although the kinetic energy increase with the increase of magnet mass and radius, the torsional speed decreases as the magnet mass and radius become smaller. Hence there exist an optimum magnet mass and radius to maximize kinetic energy.

TABLE OF CONTENTS

LIST OF FIGURES

LIST OF TABLES

CHAPTER 1

INTRODUCTION

Composite materials have exceptional properties, including: high strength to weight ratio, corrosion resistance, design flexibility and low thermal conductivity. Composites have a wide range of applications in such areas as building, bridges, aircraft, wind energy and other structures such as swimming pool panels and storage tanks. In order to further enhance the properties of composites, it is necessary to identify the deformation mechanisms in composites in various application.

1.1 Methods to Improve Interfacial Shear Strength of Composites

Carbon fibers are one of the most important high-performance fibers because of properties such as high strength to weight ratio, electrical conductivity; they are used in numerous engineering applications, such as carbon fiber composites (Tang and Kardos, 1997) in airliners (Williams and Starke Jr, 2003; Soutis, 2005), wind energy (Pimenta and Pinho, 2011), and actuators (Liu et al., 2015; Mu et al., 2016). The steady increase of the use of fiber reinforced polymer composites in commercial and military aerospace, automotive, offshore drilling, sports equipment, and various light-weight structures has driven the continuous development of novel composite materials and manufacturing techniques. However, their compressive strength is approximately only half of the tensile strength due to failure in composites. Composites fail in three modes under longitudinal compression load. These modes are: fiber failure (microbuckling or kinking), matrix failure, and interface debonding (Budiansky and Fleck, 1993; Nofar et al., 2009; Patel et al., 2016; Swolfs et al., 2015; Talreja, 2016; Safaei et al., 2015; Eftekhari and Fatemi, 2015; Faes et al., 2015; Ngah and Taylor, 2016; Agrawal et al., 2014). The stiffness and strength of the overall composites will be improved as the matrix stiffness and the strength of the matrix surrounding a fiber, and fiber/matrix interfacial strength increase. Interface acts as an efficient transmission agent of forces between fiber and matrix, and the matrix is responsible for shear load transfer. Mechanical behavior at the interface with a thickness approximately 100 nm or less plays a determinant role in stiffness and transverse strength of fiber reinforced composites. The failure or delamination of a glass fiber takes place in the matrix 3 nm away from the fiber surface was experimentally observed by angular dependent x-ray photoelectron spectroscopy (Swadener et al., 1999). In 2003, polymer coating around single-walled carbon nanotube (SWNT) was observed by scanning electron microscope (SEM) while fracture happened during SWNT pulling out of polycarbonate (Ding et al., 2003). As a result, modifying mechanical properties of polymer matrix, fibers or interface has potential to improve the strength of composites.

Raman Spectroscopy was used to investigate the interfacial micromechanics of carbon fibers in thermoplastic matrices by determining the distribution of interfacial shear stress along fibers in a single-fiber model composite (Huang and Young, 1996). There is approximately a linear variation of fiber strain from the fiber end to other locations of the fiber; this indicates that frictional shear dominates stress transfer from matrix to fiber. The maximum values of interfacial shear strength of fibers in a thermosetting epoxy resin matrix are higher than those of the same fiber reinforced poly methyl methacrylate(PMMA) and polycarbonate (PC) model composites. The possible reasons for such low values of interfacial shear stress in thermoplastic systems are the effect of residual solvent and the lack of chemical bonding between the fiber and matrix. Mechanical interlocking can primarily lead to interfacial adhesion in the composites, and preparing composites at higher temperatures can help enhance interfacial adhesion. It was found that thermal mismatch between fiber and matrix results in radial pressure on the fiber, it contributes to the maximum interfacial shear stress in the PMMA model composite.

Recently, numerous efforts have been made to improve the interfacial shear strength using CNTs grafted onto glass or carbon fibers (Mei et al., 2010; Thostenson et al., 2002; Qian et al., 2010a,b; Zhang et al., 2009a; Zeng et al., 2010; Zhao and Huang, 2010). Polyhedral oligomeric silsesquioxanes (POSS), an emerging new chemical technology for nano-reinforced organic-inorganic hybrids, has been used to graft around fibers, and the interfacial shear strength increases by 61% (Zhao and Huang, 2010). Single fiber fragmentation method was used to investigate the interfacial shear strength of CNTs coated carbon fiber embedded in epoxy matrix, and showed improvement of interfacial shear strength (Sager et al., 2009). Randomly oriented multiwall nanotubes (MWNTs) aligned carbon fiber embedded in epoxy can provide 71% of increase in interfacial shear strength, which is very high compared with 11% increase in interfacial shear strength for radially grown on MWNTs on carbon fibers in epoxy. The reason is that randomly oriented MWNTs with potentially higher percentage of MWNTs forming $\pm 45°$ angles with respect to principal stress directions under pure shear loading. However, a significant reduction in tensile strength and modulus of composites was reported. It was observed that the tensile strength of CNTs grafted on carbon fibers provide 69 % increase in strength in comparison with that of untreated carbon fibers (Sharma and Lakkad, 2011).

Electrophoresis technique is used to selectively deposit multi- and single walled CNTs on woven carbon fabric. 27% enhancement of interlaminar shear strength and a significant improvement of out-of-plane electrical conductivity are observed by introduction of 0.25 % of MWNTs in the carbon fiber/epoxy composites (Bekyarova et al., 2007). An increase of interfacial shear strength is also reported by modifying carbon fiber surface (He et al., 2010; Li, 2008; Moon et al., 1992), the treatments include oxygen plasma, nitric acid, and electrochemical oxidation. Improvement in interfacial shear strength can be also achieved by dispersing regular and functionalized CNTs in epoxy resin (Zhu et al., 2012, 2003; Che et al., 2009; Ma et al., 2009; Martinez-Rubi et al., 2011; Sui and Wagner, 2009). Many other research groups have used CNT fiber itself to evaluate the interfacial shear strength (Ganesan et al., 2011; Özden Yenigün et al., 2012; Zu et al., 2012). Dispersion of SWNT-COOH in epoxy to fabricate SWNT-COOH/epoxy/CF composites by vacuum assisted resin transfer molding technique produces 40% enhancement of shear strength for only 0.5 wt% of SWNT-COOH (Bekyarova et al., 2007). Introducing MWNT into composites can increase interfacial shear strength up to 33%. Recently, using CNT to wrap on carbon fiber then embed into epoxy was proposed to improve interfacial shear strength of carbon fiber reinforced composite. The improved mechanical performance and 40% enhancement of shear strength are observed by incorporation of SWNT-COOH from mechanical tests. Electrical conductivity of covalently integrated epoxy composites improves by modifying functionalizing CNTs by plasma (Tseng et al., 2007; Cheng et al., 2010). Modifying the interlaminar interface is an another approach to improve interfacial shear strength, and introduction of MWNT into composite can result in 33% incensement in the interfacial shear strength during fabricating the hybrid MWNT/glass/epoxy composites (Fan et al., 2008; Tsotsis, 2009). Moreover, incorporating CNT in thermoset and thermoplastic resin can also help improve electrical and thermal conductivity (Assael et al., 2008; Cheng et al., 2010; Kotaki et al., 2006).

In an effort to avoid degrading tensile properties of fibers due to grafting CNTs, Godara et al. deliver CNTs to the fiber surface by dispersing CNTs in the fiber sizing formulation, which does not introduce any damage to the fibers (Godara et al., 2010, 2009). Nanoindentation is carried on to characterize interfacial shear strength for three different categories samples that CNTs are introduced in three ways: (1) in the matrix, (2) in the fiber sizing and (3) in the fiber sizing and matrix simultaneously. Results show that interfacial shear stress increases for all three cases, and 90% incensement in interfacial shear stress is observed for composites where CNTs are introduced solely in the fiber sizing. They also find that the thermal expansion decrease by 32% by presenting double-walled CNTs into epoxy systems and 80% incensement in fracture toughness for introducing multi-walled CNTs into epoxy resin modified by a compatibilizer. The possible reason for decrease in thermal expansion is that the reduced size and higher interaction CNTs block the mobility of the polymer network and introduce microstructural rigidity. Chemically modifying nanotube surface can help dramatically improve interfacial shear strength between a single CNTs and a polymer matrix by conducting pulling out single CNTs using atomic force microscopy (AFM) tip, though the data scatter is very high (Barber et al., 2006, 2003).

Dr. Lu, et al. have put forward a new robust method to wrap CNT sheet around carbon fiber and then infiltrate into epoxy (Lu et al., 2017). The carbon fiber and the inner ply of the MWNT sheet will adhere to each other through van der Waals forces. Polymer will infiltrate into the mesoporous outer layers of the MWNT piles. These outer MWNT plies have MWNT connected to each other to form a MWNT aerogel (or xerogel after densification in liquid) with very high specific surface area (Aliev et al., 2009) before infiltration by polymer. The polymer will penetrate the mesopores and crosslink with MWNTs during infiltration of the polymer. The performed MWNT aerogel are found to be dispersed evenly in the polymer to reinforce the fiber/polymer interface. In order to characterize the interfacial adhesion of carbon fiber reinforced composites, measurement techniques, such as single-fiber fragmentation test, single fiber push out test, microbond test, and fiber push-in test are conducted to measure fiber/matrix interfacial shear strength (Xu, 2017). Finite element simulation is conducted to analyze the stress distribution of composites with and without nanocomposites using data from nanoindentation. Result shows that nanocomposites in composites makes stress distribution smooth. Fiber push out test shows that interfacial shear strength of CNT/carbon fiber reinforced composite is 81% higher than that of carbon fiber reinforced composite, and fiber push in test shows 87% improvements.

1.2 Buckling Analysis of A Composite Under Compression

Low-density, high strength composite materials play a critical role in a wide range of areas including aerospace, defense, sports, transportation, and renewable energy. These materials are beneficial for providing improved energy efficiency, easier mobility, agility, and desirable aesthetics. The high tensile strength is derived from fibers impregnated in the polymer matrix. Carbon fibers are one of the most popular fibers due to its high strength to weight ratio, electrical conductivity, corrosion resistance and high thermal conductivity in some forms, making carbon fibers it a promising solution to numerous engineering applications, such as actuators (Liu et al., 2015; Mu et al., 2016), and reinforced fiber in polymer matrix (Tang and Kardos, 1997), which is now used as the primary structural materials for large airliners (Williams and Starke Jr, 2003; Soutis, 2005), and is used increasingly in other applications, such as wind energy (Pimenta and Pinho, 2011). However, the compressive strength of composites is in general much lower than tensile strength due to the fact that under compression, the fibers tend to fail in micro-buckling (or kinking) before compressive fracture occurs (Hahn and Sohi, 1986; Steif, 1987; Tadjbakhsh and Wang, 1992; Schultheisz and Waas, 1996; Waas and Schultheisz, 1996; Kyriakides et al., 1995; Yongbo and Huimin, 2011; Harich et al., 2009; Ji and Waas, 2007; Waas et al., 1990). An analytical model to predict the compressive strength was first proposed by Rosen (Rosen, 1965) for compressive behavior of unidirectional composites. Subsequently, many different models were developed to estimate compressive strength of composite. Based on Rosen's work, 3D analysis was conducted and the numerical result of aluminum and steel fiber reinforced epoxy was consistent with experiment results, but not for graphite/epoxy and boron/epoxy (Greszczuk, 1975). Unknown boundary conditions of the microbuckled region and initial misalignment were also accounted by introducing factors in Rosen's model (Lo and Chim, 1992; Yeh and Teply, 1988). Fiber-matrix bond condition and matrix slippage was considered in the model (Xu and Reifsnider, 1993) where fiber was assumed as a beam resting on elastic foundation. Theory of elasticity was used to solve micro-buckling problem and finite element method was carried out to verify theoretical result (Zhang and Latour Jr, 1994). Some recent papers on fiber micro-buckling problem are presented in (Lapusta et al., 2008; Bai et al., 2016; Su et al., 2012; Parnes and Chiskis, 2002; Lapusta et al., 2011; Andrianov et al., 2012). In analysis the fibers are considered as isotropic. In practise, not all fibers are isotropic especially carbon fibers. Transverse properties of carbon fiber were measured using Raman spectroscopy, nanoindentation, and micromechanics methods (Luo et al., 2012; Maurin et al., 2008; Miyagawa et al., 2005), they are in general lower than the properties in the axial direction. In addition, fiber misalignment and matrix yield are known to influence compressive strengths in unidirectional composites (Roy et al., 2005, 2007).

In order to properly study compressive strength of composite, researchers focused on investigating the fiber/matrix interface. In this process, a finite interphase region was assumed to exist between fiber and matrix (Waas, 1992; Maligno et al., 2010; Drzal, 1990; Lane et al., 2001). Most of the above theoretical work considered an interface rather than interphase region, which is a layer of material between carbon fiber and matrix that could help improve matrix dominated properties such as interfacial shear strength and compressive strength. Recently, introduction of interphase region between fiber and matrix have been observed to improve compressive strength (Zhang et al., 2009a). The grafting of CNTs (CNTs) onto the carbon fiber carbon fibers through chemical vapor deposition can improve the interfacial shear strength, resulting in IFSS 150% higher than that of composite without CNTs. However, this technique usually leads to a degradation of carbon fiber in-plane properties due to processing at high temperature. As an alternative, a novel method was introduced in (Lu et al., 2017) where carbon fiber was wrapped by MWNT sheet and then impregnated into a polymer matrix, producing a nanocomposites layer in the interphase region. In this work, the compressive failure of a polymer matrix composite containing unidirectional carbon fiber with interphase region is investigated. In the study, the fiber is considered as anisotropic, and the interphase region and the matrix are considered as isotropic. The results obtained by modeling the fiber as an anisotropic and linearly elastic material are compared with those obtained from isotropic fiber study. We also focus on the effect of mechanical properties and thickness of interphase region on the compressive strengths. FEM simulations were carried out to verify the theoretical work.

1.3 Composite Actuator

Baughman et al. (Baughman et al., 1999) first find that injecting charge to nanotubes, nanotubes can exhibit mechanical deformation. Layered Nafion/single-walled CNT composites actuator is investigated and large mechanical response at low voltages without the use of an electrolyte are reported (Levitsky et al., 2004). Later, nanotubes was dispersed into the polymer matrix to serve as an embedded network of electrodes to enhance the actuation response (Landi et al., 2005). The reason for the best performance of nanotube/Nafion actuators is that nanotubes uniformly distribute (Lee et al., 2007). CNTs is introduced to electroactive polymer matrix, and the actuation performance is much better than embedded into pristine polymer. Higher strains can be maintained in electroactive polymer actuators and enhanced electrochemical efficiency in the actuation is found due to enhancement of conductivity (Zhang et al., 2005; Tahhan et al., 2003). Another electromechanical composite actuator is made by adding very low (∼0.01%) concentration of CNTs into nematic liquid-crystalline elastomers (Courty et al., 2003). Ply actuators is developed by casting an epoxy layer onto the surface of a random bucky-paper. Such actuator exhibit higher stiffness and strength than previous bucky-paper actuators (Yun et al., 2005). Same group also study to use carbon nanofibers as actuator material in both liquid and solid electrolytes (Yeo-Heung et al., 2006a,b).

Ultraviolet light illumination can deform and fix the polymers containing cinnamic groups into predetermined shapes-such as tubes, arches, spirals or elongated films. The stability of these new shapes is extremely good, even keeping stable when heated up to $50°C$, and recovering to their original shape can be achieved at room temperature when exposed to ultraviolet light of a different wavelength. The excellent ability of such polymers to deform to desired shapes and then recover their primitive shape when subjected to remote light activation can result in diverse applications (Lendlein et al., 2005). Twisted-spun multi-wall CNTs can do actuation in response to voltage ramps and potentiostatic pulses (Mirfakhrai et al., 2007). Actuation strain can be up to 0.5 % when the applied potentials is 2.5 V. Actuator made of CNT polyimide composite (Sellinger et al., 2010) can bend upward due to thermal expansion when the temperature is below its T_g ($220°C$). And polymer become soften and bends downward due to gravity when the temperature is above glass transition. Nanofiber hydrogel actuator is fabricated by introducing an anisotropic structure into the nanofiber gel. pH changes can result in bending and stretching motions of nanofiber hydrogel actuator. The motions of bending and stretching of such actuator are very stable over a constant period and displacement (Nakagawa et al., 2011).

Hybrid CNT yarn muscles can perform torsional and tensile actuation when subjected to electrical, chemical and photonic stimulus (Lima et al., 2012). Fast, high-force, large strokes torsional and tensile actuation can be realized by using guest-filled, twist-spun CNT yarns. Guest dimensions can be changed during electrical, chemical, or photonic excitation. They demonstrate more than a million tensile and torsional actuation cycles, wherein a muscle delivers 3% tensile contraction at 1200 cycles/minute or spins a rotor at an average 11,500 revolutions/minute. A new electroactive actuators is devised by using ionic liquids and self-assembled sulphonated block copolymers. It shows enhancement in actuation properties and large generated strain (up to 4%) without any signs of back relaxation. The ability of millimeter-scale displacements at sub-1-V conditions over 13500 cycles in air with rapid response (< 1 s) has been reported (Kim et al., 2013). Researchers embed aligned CNTs into paraffin wax on polyimide substrate and then actuate it by visible-light. The actuator can bend too three dimensional helical buckling controlled by tuning the CNT alignment direction. The response time of photomechanical actor is milliseconds and no detectable fatigue is found after reversibly performing 10000 cycles (Deng et al., 2015).

Another polymer coated CNT yarn artificial muscle is devised by Dr. Baughman's group, and this types of artificial muscle have higher performance than guest filled artificial muscle. In this study, we study the mechanism of this type of artificial muscle. We predict the effect of polymer thickness to core diameter ratio on the absorption-driven torsional actuation of a polymer coated CNT yarn. We also predict the tensile stroke and isobaric contractile work capacity of coiled polymer coated CNT yarn artificial muscles and polymer infiltrated CNT yarn artificial muscles.

CHAPTER 2

MODELING THE COMPRESSIVE BUCKLING LOAD AS A FUNCTION OF THE INTERPHASE THICKNESS IN A CARBON NANOTUBE SHEET WRAPPED CARBON FIBER COMPOSITE

2.1 CNT/CF Laminate Composites and Surface Wettability

An initial setup for the fabrication of CNT/carbon fiber with a bias angle of 0° composite samples are developed through a rolling process. In this process, three layers of CNT forests are placed vertically aligned with a roll of manually spread Hexcel IM7 carbon fiber tow. CNT sheets are pulled out from the forests and attached over the carbon fiber tow at the rotating mandrel at a speed of about 72 rpm. Spreading Hexcel IM7 on CNT sheets with a stacking angle of either 45° or 90° is conducted manually. Then ethanol is used to densify them. SEM images of carbon fiber and carbon fiber/CNT with a bias angle (0°, 45°, or 90°) are shown in Figure 2.1. Then all samples are embedded in epoxy matrix by vacuum assisted resin infusion process. For these samples, vacuum bagging starter kit (model 947) from Composite Envisions is used Figure 2.2. In order to make sure that no bubbles are trapped in the laminate, mixing time of Epon 862 is controlled and vacuum is used during curing.

After 24 hours, epoxy is fully cured, four types of samples are obtained: unidirectional carbon fibers embedded in epoxy, CNT/CF with a bias angle (0°, 45° ,or 90°) composite. Strong interfacial adhesion between fiber and matrix plays an important role in successful usage of fiber composite. However, carbon fiber often shows poor adhesion to epoxy due to its relatively inert and non-polar fiber surface. The perfect surface wetting contributes to good interfacial adhesion, which can be improved by modifying the property of carbon fiber surface (Xu et al., 2008). Scanning electron microscope (SEM) images of the cross sectional views of CF/epoxy composite after breaking it with liquid nitrogen, making the samples more

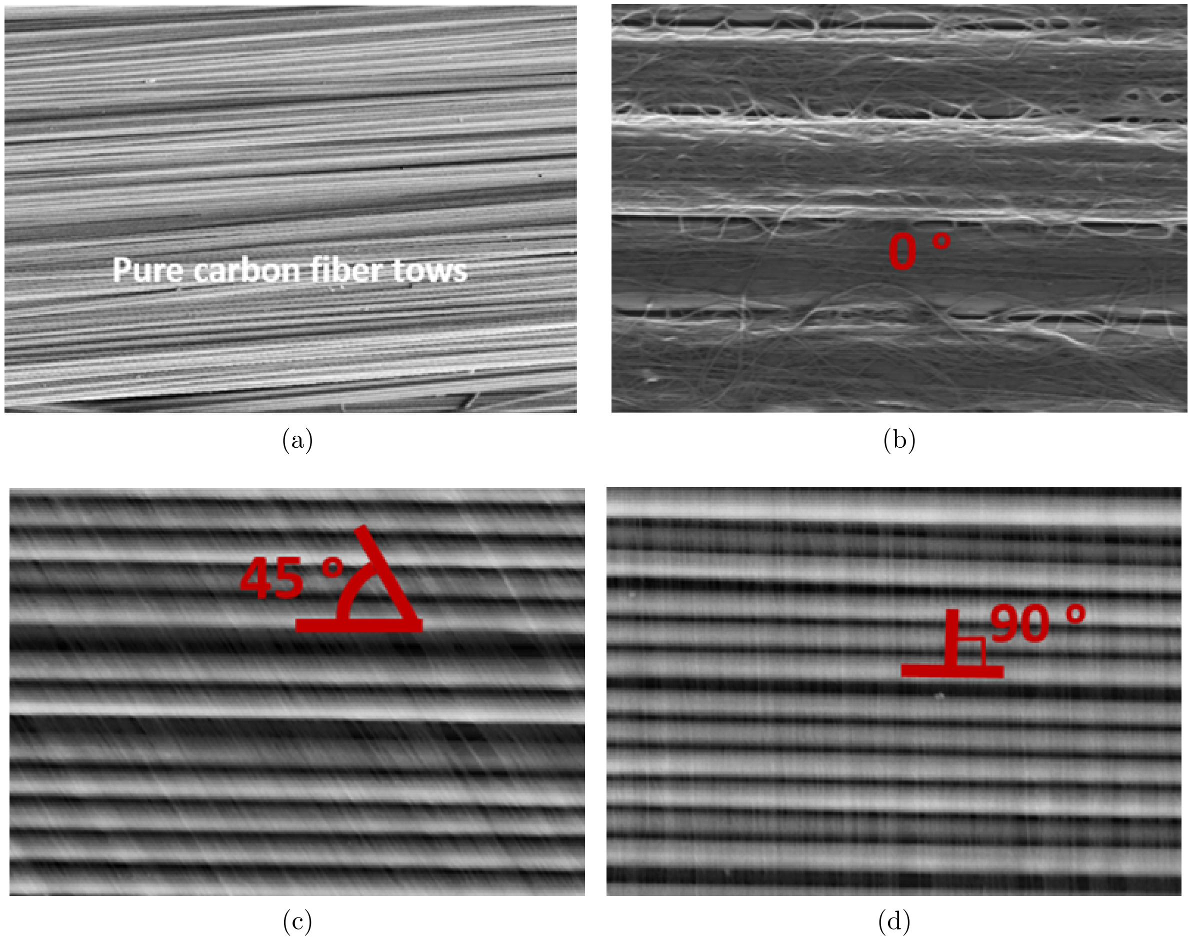

Figure 2.1: Pure carbon fiber and CNT/carbon fiber with different bias angles. (a) Pure carbon fiber tows with fiber diameter around 5 μm. (b) SEM images of CNT/carbon fiber with bias angle 0° after densification by ethanol. (c) SEM micrograph showing CNT/carbon fiber with bias angle 45° after densification by ethanol. (d) SEM micrograph showing CNT/carbon fiber with bias angle 90° after densification by ethanol.

brittle and easy to break without changing relative position of fiber and matrix, otherwise fiber will be pulled due to its higher strength than matrix, are shown in Figure 2.3 and a very poor wettability of the epoxy on the carbon fiber is observed. CNT/CF with bias angle of 0° laminate is also breaking using liquid nitrogen, SEM micrographs of the cross section show very good wettability of the epoxy on the carbon fibers in Figure 2.4.

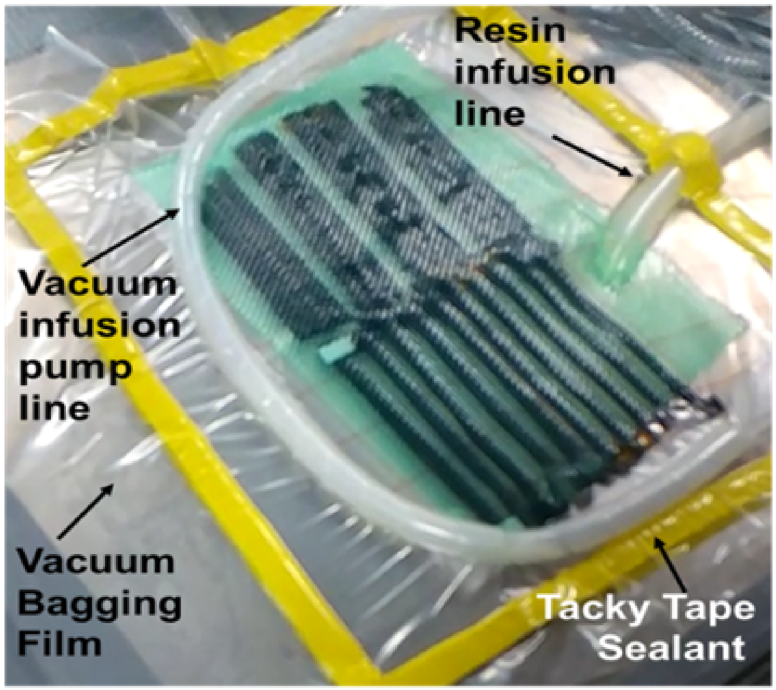

Figure 2.2: Vacuum resin infusion of carbon fiber tows and CNT/carbon fiber with different bias angle.

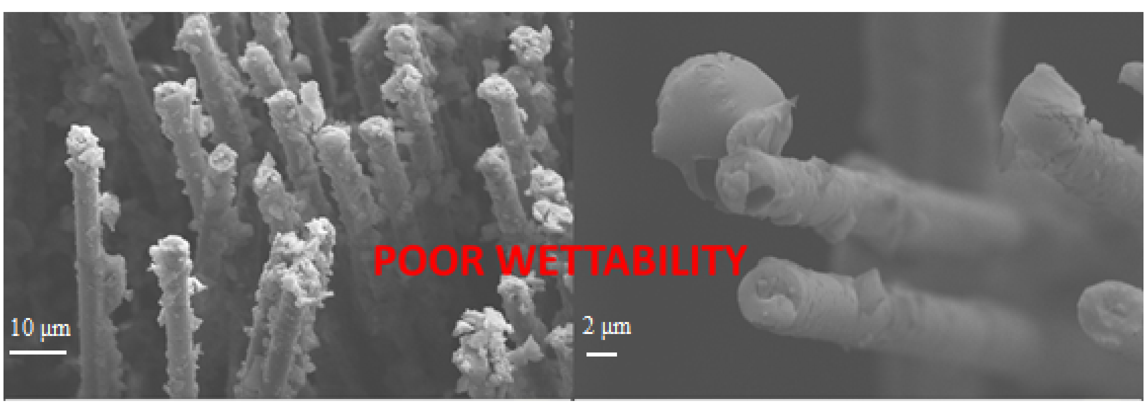

Figure 2.3: SEM images of a cross-section in a unidirectional carbon fiber epoxy after breaking it with liquid nitrogen, showing poor wettability of epoxy on the carbon fibers. Bar scales: 10 μm (left) and 2 μm (right).

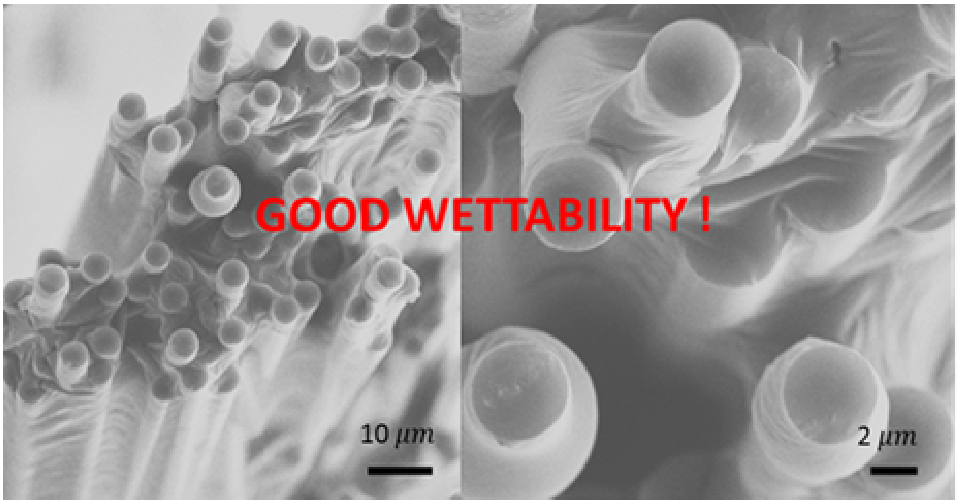

Figure 2.4: SEM images of a fracture surface of CNT/carbon fiber composite with bias angle 0°. The sample is cooled down to cryogenic temperature by using liquid nitrogen, it is subsequently subjected to bending that leads to fracture. The micrograph shows that there is a good wettability of epoxy on the carbon fibers. Bar scales: 10 μm (left) and 2 μm (right).

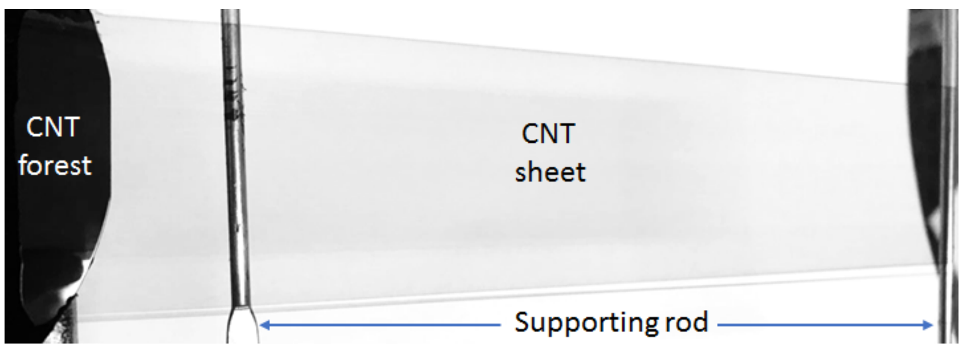

Figure 2.5: Photograph of a MWNT sheet drawn from forest.

2.2 Theoretical Analysis

The CNT sheet drawn from MWNT forest is meso-porous with high specific surface area, consequently very small amount of CNT sheet by weight can be used to wrap around large volume of carbon fibers (Lu et al., 2017). Figure 2.5 shows a self-supporting long MWNT sheet hand-drawn from a nanotube forest. Then carbon fiber is wrapped by CNT sheet. Figure 2.6a shows a schematic diagram of a MWNT sheet being wrapped circumferentially

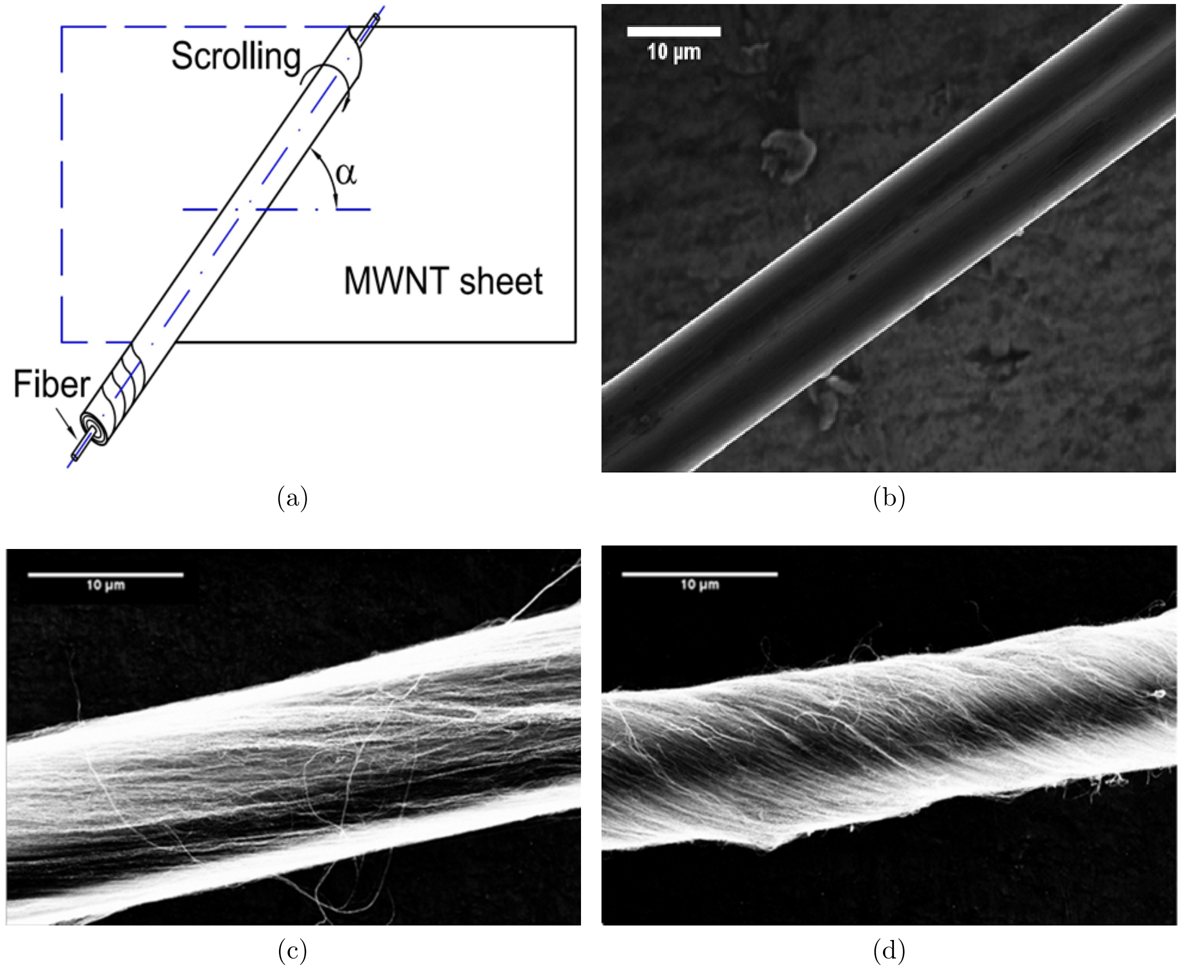

(a) (b) (c) (d)

Figure 2.6: CNT sheet wrapping carbon fiber. (a) A schematic diagram showing a MWNT scrolling a carbon fiber (Xu, 2017). (b) SEM images of single carbon fiber (Xu, 2017). (c) SEM micrograph showing segment of the single carbon fiber with 30° wrapping bias angle (Xu, 2017). (d) SEM micrograph showing segment of the single carbon fiber with 45° warp bias angle (Xu, 2017).

on a carbon fiber at a wrapping angle α. The MWNT wrapped carbon fiber is then embedded into a polymer matrix. The inner ply of the MWNT sheet adheres to the carbon fiber via Van der Waals forces. Figure 2.6b shows SEM image of single carbon fiber. 30° and 45° wrap bias angle are used to wrap CNT sheet around carbon fiber respectively in Figure 2.6c and Figure 2.6d. Then CNT sheet wrapped carbon fiber is embedded into a polymer matrix, nanocomposite made of CNT sheet and epoxy is formed at this time. Figures 2.9a

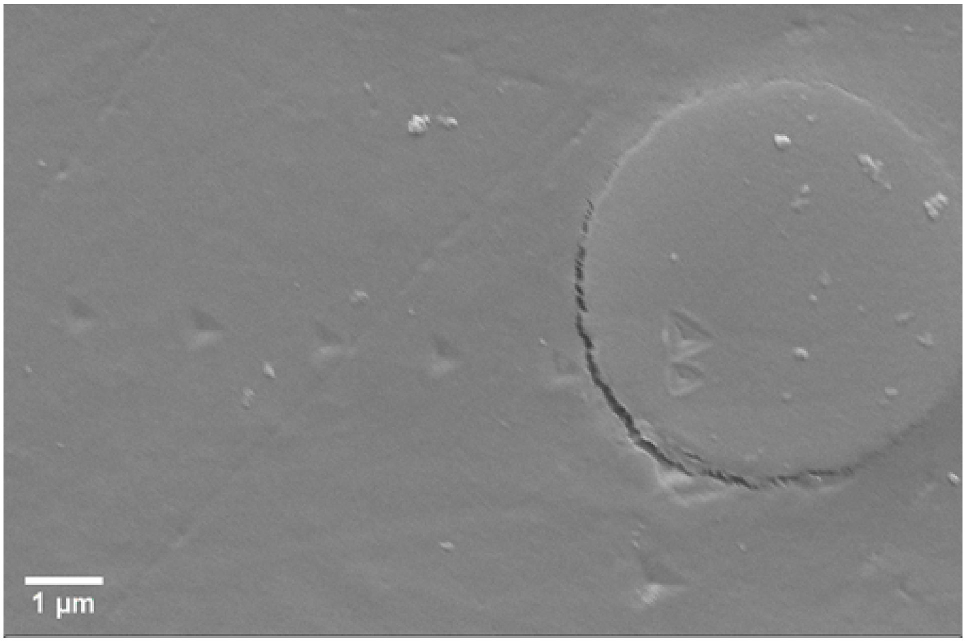

Figure 2.7: SEM images indents of composite with CNT at wrapping bias 0° (Xu, 2017).

and 2.9b show the surface topography using atomic force microscopy of neat and CNT sheet scrolled carbon fiber embedded in polymer matrix, separately. Modulus scanning using a cube corner nanoindenter tip was conducted on neat polymer matrix and on nanocomposite, which can be seen in Figure 2.7. The surface modulus increased from 3.1 GPa to 24.7 GPa for CNT sheet wrapping carbon fiber at a wrapping angle 0°, and 13.2 GPa for CNT sheet wrapping carbon fiber at a wrapping angle 45° as shown in Figure 2.8. Based on these experiments, the theoretical model was built to analyze the optimum thickness of nanocomposite interphase region. The composite consists of three constituents:fiber, nanocomposite (interphase region), and matrix. Figure 2.10 shows a schematic diagram of the three regions in a CNT wrapped carbon fiber composites. Fiber was modeled as transversely isotropic, and nanocomposite and matrix (e.g., epoxy) were modeled as a isotropic elastic continuum respectively. If the volume fraction of reinforcement is low and fibers do not interact, the problem can be simplified to that a single fiber coated with MWNT sheets rest in an infinite matrix. A schematic graph is shown in Figure 2.10. We assumed that the fiber/interphase

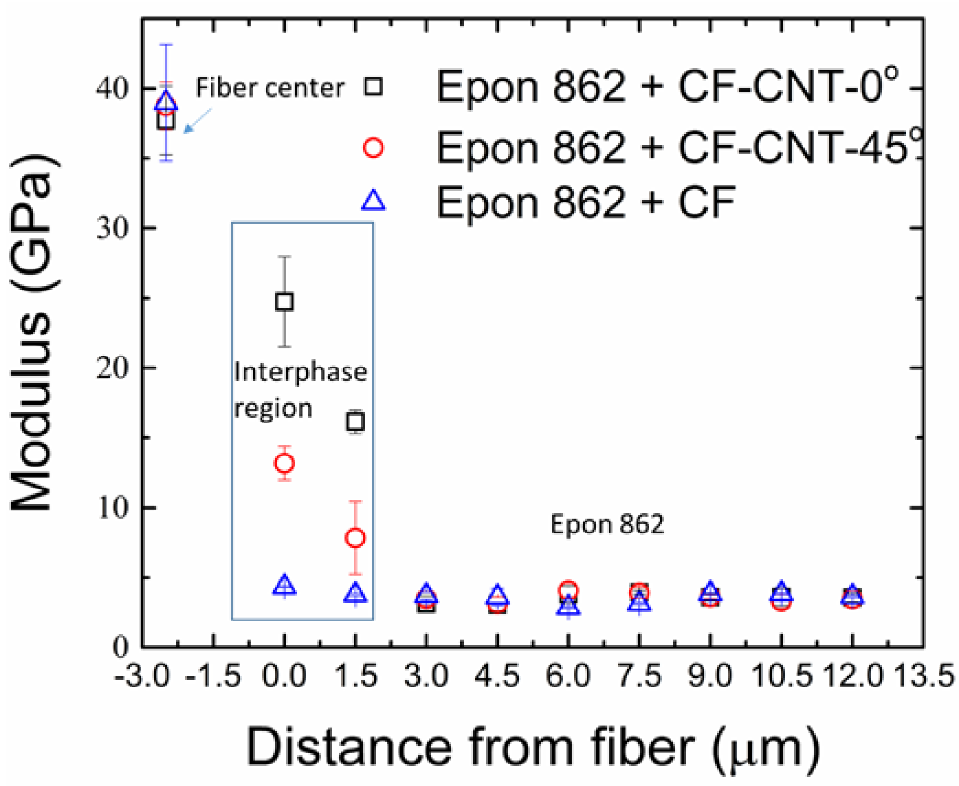

Figure 2.8: Young's modulus of nanocomposites and matrix (Xu, 2017).

region and interphase region/matrix interfacial bonds are perfect, so that displacement and force are continuous on the interfacial boundary. The composite is subjected to a plane strain deformation in the x-y plane. Subscripts of 1, 2, 3 represent fiber, interphase, and matrix, respectively. The entire composite laminate is assumed to be compressed by rigid platens in the fiber direction.

From the uniformly strained state to the perturbed state, two deformation modes of the fiber are possible. In this work, as the fiber's modulus is assumed to be significantly higher than that of matrix, anti-symmetric mode prevails according to previous studies (Waas et al., 1990; Novozhilov, 1999). The fiber displacement with the perturbation should satisfy anti-symmetrical conditions.

$$
\begin{aligned}
u_1(x_1, y_1) &= -u_1(x_1, y_1) \\
v_1(x_1, y_1) &= v_1(x_1, -y_1)
\end{aligned}
\tag{2.1}
$$

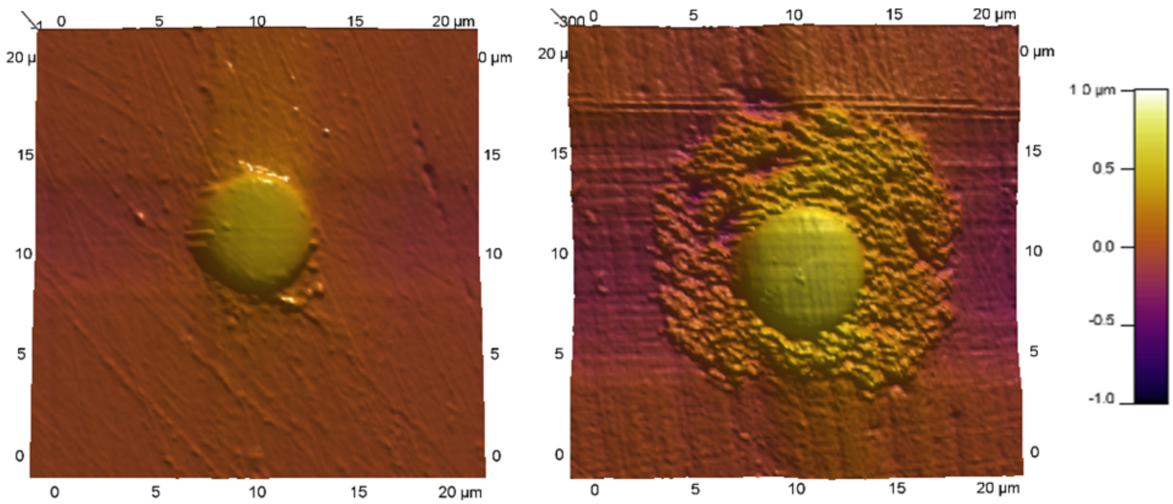

(a) (b)

Figure 2.9: Surface topographs taken by atomic force microscopy of (a) Carbon fiber (Xu, 2017). (b) MWNT scrolled carbon fiber when embedded in polymer matrix after polishing (Xu, 2017).

At first, when an aligned fiber/CNTs-reinforced composite is subjected to a uniaxial uniformly strain, the corresponding stress in dimensionless form for the interphase region and matrix is given by $s_i = \sigma/2G_i$,(i = 2,3), where σ_{x_i} is the stress in the x_i direction, and G_i is the shear modulus. Note that $i = 1$ denotes fiber, i=2 denotes matrix/CNT interphase region, and $i = 3$ denotes matrix. When the fiber is assumed to be transversely isotropic, the number of independent material constants reduces to five. The five independent material constants used in this paper are:E_{fx_1}, E_{fy_1}, $G_{x_1y_1}$, $\nu_{x_1y_1}$, and $\nu_{y_1z_1}$. Equilibrium equations for the solid with small perturbation are well documented (Novozhilov, 1999). Neglecting body force, the equilibrium equations governing the incremental stresses due to the perturbation are

$$\begin{aligned}
&\frac{\partial(\sigma_x - \omega_z\sigma^0_{xy} + \omega_y\sigma^0_{xz}}{\partial x} + \frac{\partial(\sigma_{xy} - \omega_z\sigma^0_{y} + \omega_y\sigma^0_{yz})}{\partial y} + \frac{\partial(\sigma_{xz} - \omega_z\sigma^0_{yz} + \omega_y\sigma^0_{z})}{\partial z} = 0 \\
&\frac{\partial(\sigma_{xy} - \omega_x\sigma^0_{xz} + \omega_z\sigma^0_{x})}{\partial x} + \frac{\partial(\sigma_{y} - \omega_x\sigma^0_{yz} + \omega_z\sigma^0_{xy})}{\partial y} + \frac{\partial(\sigma_{yz} - \omega_x\sigma^0_{z} + \omega_z\sigma^0_{zx})}{\partial z} = 0 \\
&\frac{\partial(\sigma_{xz} - \omega_y\sigma^0_{x} + \omega_x\sigma^0_{xy})}{\partial x} + \frac{\partial(\sigma_{yz} - \omega_y\sigma^0_{xy} + \omega_x\sigma^0_{y})}{\partial y} + \frac{\partial(\sigma_{z} - \omega_y\sigma^0_{xz} + \omega_x\sigma^0_{yz})}{\partial z} = 0
\end{aligned} \tag{2.2}$$

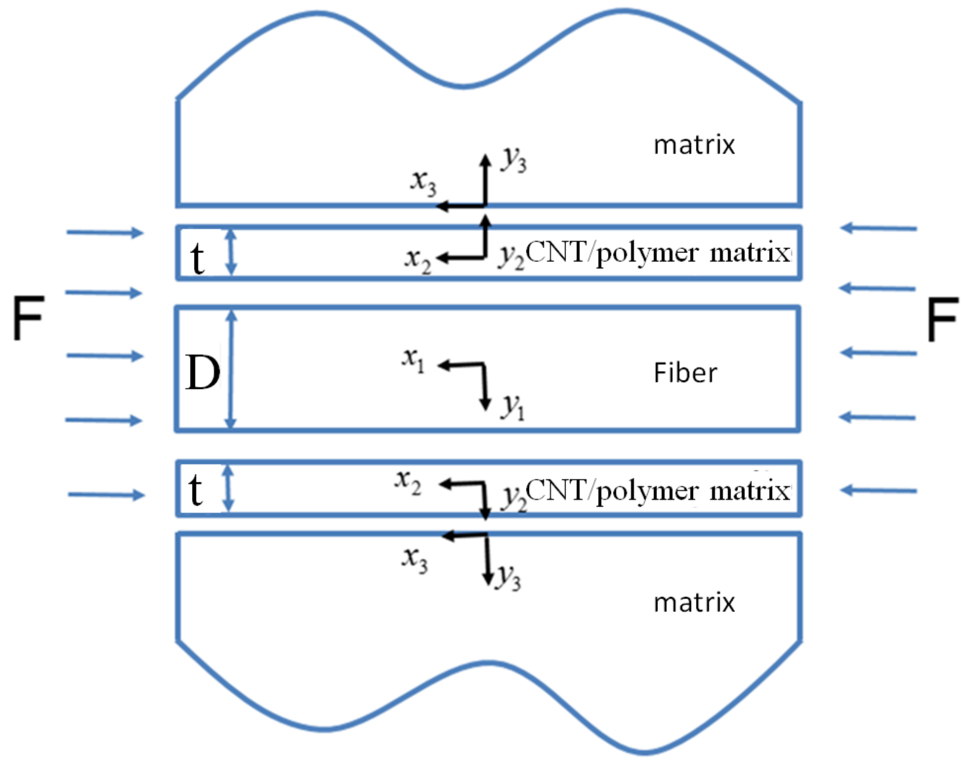

Figure 2.10: Configuration of composite under compression in fiber direction.

In Equation (2.2), superscript '0' denotes the original state and symbols without superscript represent the perturbed state. Here $\omega_z = \frac{1}{2}(\frac{\partial u}{\partial y} - \frac{\partial v}{\partial x})$, $\omega_x = \omega_y = 0$, due to the fact plain strain problem is assumed where u, v are independent of z, and ω is zero. With the nonzero components $\sigma_x^0 =$ -σ_x the above equations simply to the following equations

$$\begin{aligned}
&\frac{\partial \sigma_x}{\partial x} + \frac{\partial \sigma_{xy}}{\partial y} + \frac{\partial \sigma_{xz}}{\partial z} = 0 \\
&\frac{\partial(\sigma_{xy} - \omega_z \sigma_x)}{\partial x} + \frac{\partial \sigma_y}{\partial y} + \frac{\partial \sigma_{yz}}{\partial z} = 0 \\
&\frac{\partial \sigma_{xz}}{\partial x} + \frac{\partial \sigma_{yz}}{\partial y} + \frac{\partial \sigma_z}{\partial z} = 0
\end{aligned} \tag{2.3}$$

In the next step, Equation (2.3) and strain displacement relationships $\varepsilon_x = \frac{\partial u}{\partial x}$, $\varepsilon_y = \frac{\partial v}{\partial y}$, ε_{xy} $= \frac{1}{2}(\frac{\partial v}{\partial x} + \frac{\partial u}{\partial y})$ are applied to fiber, interphase region and matrix individually.

2.2.1 Governing Equations for Carbon Fibers

The fiber is assumed to be homogeneous and transversely isotropic solid. Interphase region and matrix are assumed to be homogeneous and linearly isotropic solids. Constitutive equations for transversely isotropic fiber are given by

$$\begin{bmatrix} \sigma_{x_1} \\ \sigma_{y_1} \\ \sigma_{z_1} \end{bmatrix} = \begin{bmatrix} \frac{(-\upsilon_{y_1z_1}^2+1)E_{fx_1}}{\Delta} & \phi & 0 \\ \phi & \frac{(1-\upsilon_{y_1x_1}\upsilon_{x_1y_1})E_{fy_1}}{\Delta} & 0 \\ 0 & 0 & 2G_{x_1y_1} \end{bmatrix} \begin{bmatrix} \varepsilon_{x_1} \\ \varepsilon_{y_1} \\ \varepsilon_{z_1} \end{bmatrix} \tag{2.4}$$

where $\Delta = (\upsilon_{y_1z_1}+1)(1-\upsilon_{y_1z_1}-2\upsilon_{y_1x_1}\upsilon_{x_1y_1})$, $\phi = \frac{(1+\upsilon_{y_1z_1})\upsilon_{y_1x_1})E_{fx_1}}{\Delta}$.

Equation (2.4) and strain displacement relationships are substituted into Equation (2.3) , yielding the following equations

$$\begin{aligned} &\frac{(1-\upsilon_{y_1z_1}^2)E_{fx_1}}{\Delta}\frac{\partial^2 u_1}{\partial x_1^2} + G_{x_1y_1}\frac{\partial^2 u_1}{\partial y_1^2} + (G_{x_1y_1}+\phi)\frac{\partial^2 v_1}{\partial x_1 y_1} = 0 \\ &(G_{x_1y_1} - \frac{\sigma_{x_1}}{2})\frac{\partial^2 v_1}{\partial x_1^2} + \frac{(1-\upsilon_{y_1x_1}\upsilon_{x_1y_1})E_{fx_2}}{\Delta}\frac{\partial^2 v_1}{\partial y_1^2} = 0 \end{aligned} \tag{2.5}$$

Displacements of fiber are antisymmetric about x_1, and therefore Equation (2.5) has a solution of the form,

$$\begin{aligned} u_1(x_1,y_1) &= f(y_1)sin(\alpha x_1) \\ v_1(x_1,y_1) &= g(y_1)cos(\alpha x_1) \end{aligned} \tag{2.6}$$

where $\alpha = 2\pi/\lambda_w$ and λ_w is the buckle wavelength. Then, substituting Equation (2.6) into Equation (2.5) and elimination of $g(y_1)$ result in the following ordinary differential equation for $f(y_1)$

$$a_1\frac{\partial^4 f(y_1)}{\partial y_1^4} + a_2\alpha^2\frac{\partial^2 f(y_1)}{\partial y_1^2} + a_3\alpha^4 f(y_1) = 0 \tag{2.7}$$

Similarly, eliminating $f(y_1)$ gives an ordinary differential equation for $g(y_1)$,

$$a_1\frac{\partial^4 g(y_1)}{\partial y_1^4} + a_2\alpha^2\frac{\partial^2 g(y_1)}{\partial y_1^2} + a_3\alpha^4 g(y_1) = 0 \tag{2.8}$$

where the a_1, a_2, a_3 are constants, given as:

$$\begin{aligned}
&a_1 = -G_{X_1Y_1}\tfrac{(1-\upsilon_{y_1x_1}\upsilon_{x_1y_1})E_{fx_1}}{\Delta}\\
&a_2 = \tfrac{(1-\upsilon_{y_1x_1}\upsilon_{x_1y_1})(1-\upsilon_{y_1z_1}^2)E_{fx_1}E_{fy_1}}{\Delta^2} - G_{x_1y_1}\sigma_{x_1} - \tfrac{\sigma_{x_1}}{2}\\
&-2G_{x_1y_1}\phi - \phi^2\\
&a_3 = \tfrac{(-1+\upsilon_{y_1z_1}^2)E_{fx_1}}{\Delta}(-\tfrac{\sigma_{x_1}}{2} + G_{x_1y_1})
\end{aligned} \tag{2.9}$$

The solutions of Equation (2.7) and Equation (2.8) become

$$\begin{aligned}
u_1(x_1, y_1) &= (-B_1 + k_1D_1)sinh(\beta_1\alpha y_1)sin(\alpha x_1)\\
v_1(x_1, y_1) &= (B_1m_1 + D_1)cosh(\beta_1\alpha y_1)cos(\alpha x_1)
\end{aligned} \tag{2.10}$$

Here $\beta_1 = \sqrt{-\frac{a_2}{2a_1} + \sqrt{a_2^2 - 4a_1a_3}}$ and k_1 and m_1 are calculated by the following equations

$$\begin{aligned}
m_1 &= (\tfrac{(1-\upsilon_{y_1z_1}^2)E_{fx_1}}{\Delta} - G_{x_1y_1}\beta_1^2)/((G_{x_1y_1} + \phi)\beta_1)\\
k_1 &= (G_{x_1y_1} + \phi)\beta_1/(-\tfrac{(1-\upsilon_{y_1z_1}^2)E_{fx_1}}{\Delta} + G_{x_1y_1}\beta_1^2)
\end{aligned} \tag{2.11}$$

2.2.2 Governing Equations for Interphase Region and Matrix

Hook's law for the linearly isotropic interphase region and matrix takes the form

$$\sigma_{mn} = \lambda\delta_{mn}\varepsilon_{kk} + 2Ge_{mn} \tag{2.12}$$

Here m, n, k denote x_2, y_2 and z_2 or x_3, y_3 and z_3. And λ is the *Lamé* constant, G is the shear modulus. Substitution of Equation (2.12) into Equation (2.3) yields the following equations

$$\begin{aligned}
&(\lambda_i + 2G_i)\tfrac{\partial^2 u_i}{\partial x_i^2} + G_i\tfrac{\partial^2 u_i}{\partial y_i^2} + (\lambda_i + G_i)\tfrac{\partial^2 v_i}{\partial x_i y_i} = 0\\
&(\lambda_i + 2G_i)\tfrac{\partial^2 v_i}{\partial y_i^2} + (G_i - \tfrac{\sigma_{x_i}}{2})\tfrac{\partial^2 v_i}{\partial x_i^2} + (\lambda_i + G_i + \tfrac{\sigma_{x_i}}{2})\tfrac{\partial^2 v_i}{\partial x_i y_i} = 0
\end{aligned} \tag{2.13}$$

In Equation (2.13), the index i takes the values of 2 or 3; 2 indicates the interphase region while 3 represents the matrix. A similar method is used to solve Equation (2.13), and the displacement fields for interphase region and matrix are obtained. In the interphase region, the solution is given as

$$
\begin{aligned}
u_2(x_2,y_2) &= (-B_2 sinh(\alpha y_2) - A_2 cosh(\alpha y_2) + k_2 D_2 sinh(\mu_2 \alpha y_2) + k_2 C_2 cosh(\mu_2 \alpha y_2)) sin(\alpha x_2) \\
v_2(x_2,y_2) &= (A_2 sinh(\alpha y_2) + B_2 cosh(\alpha y_2) + C_2 sinh(\mu_2 \alpha y_2) + D_2 cosh(\mu_2 \alpha y_2)) cos(\alpha x_2)
\end{aligned}
\tag{2.14}
$$

where $k_2 = \frac{\mu_2(\beta_2+0.5)}{0.5\mu_2^2-\beta_2-1}$, $\beta_2 = \frac{\lambda_2}{2G_2}$, and $\mu_2 = \sqrt{1-s_2^2}$ For matrix, the solution is

$$
\begin{aligned}
u_3(x_3,y_3) &= [B_3 e^{-\alpha y_3} - k_3 D_3 e^{-\mu_3 \alpha y_3}] sin(\alpha x_3) \\
v_3(x_3,y_3) &= [B_3 e^{-\alpha y_3} + D_3 e^{-\mu_3 \alpha y_3}] cos(\alpha x_3)
\end{aligned}
\tag{2.15}
$$

where $k_3 = \frac{\mu_3(\beta_3+0.5)}{0.5\mu_3^2-\beta_3-1}$, and $\beta_3 = \frac{\lambda_3}{2G_3}$, $\mu_3 = \sqrt{1-s_3^2}$. And B_i, D_i (i = 1, 2, 3) and A_2, C_2 are eight unknowns constants.

2.2.3 Application of Boundary Conditions

The force boundary conditions for Equation (2.3) are given below

$$
\begin{aligned}
\Delta f_x &= (\sigma_x - \omega_z \sigma^\circ_{xy} + \omega_y \sigma^\circ_{xz})\kappa + (\sigma_{xy} - \omega_z \sigma^\circ_y + \omega_y \sigma^\circ_{yz})\theta + (\sigma_{xz} - \omega_z \sigma^\circ_{yz} + \omega_y \sigma^\circ_z)\mu \\
\Delta f_y &= (\sigma_{xy} - \omega_x \sigma^\circ_{xz} + \omega_z \sigma^\circ_x)\kappa + (\sigma_y - \omega_x \sigma^\circ_{yz} + \omega_z \sigma^\circ_{xy})\theta + (\sigma_{yz} - \omega_x \sigma^\circ_z + \omega_z \sigma^\circ_{zx})\mu \\
\Delta f_z &= (\sigma_{xz} - \omega_y \sigma^\circ_x + \omega_x \sigma^\circ_{xy})\kappa + (\sigma_{yz} - \omega_y \sigma^\circ_{xy} + \omega_x \sigma^\circ_y)\theta + (\sigma_z - \omega_y \sigma^\circ_{xz} + \omega_x \sigma^\circ_{yz})\mu
\end{aligned}
\tag{2.16}
$$

The displacement and traction vectors are assumed to be continuous at the fiber/ interphase region and interphase region/matrix boundary, and the continuity conditions are given as below. At the interface between carbon fiber and CNT/matrix nanocomposite interphase region, that is, at: $y_1 = \frac{D}{2}$, $y_2 = \frac{-t}{2}$ in Figure 2.10,

$$
\begin{aligned}
u_1 - u_2 &= 0 \\
v_1 - v_2 &= 0 \\
\Delta f_{x_1} - \Delta f_{x_2} &= 0 \\
\Delta f_{y_1} - \Delta f_{y_2} &= 0
\end{aligned}
\tag{2.17}
$$

At the interface between the CNT/matrix nanocomposite interphase region and the neat resin, that is at: $y_2 = \frac{t}{2}$, $y_3 = 0$ in Figure 2.10,

$$
\begin{aligned}
&u_2 - u_3 = 0 \\
&v_2 - v_3 = 0 \\
&\Delta f_{x_2} - \Delta f_{x_3} = 0 \\
&\Delta f_{y_2} - \Delta f_{y_3} = 0
\end{aligned}
\tag{2.18}
$$

The displacement field provided in Equations (2.10), (2.14) and (2.15) and traction Equation (2.16) are substituted into Equations (2.17) and (2.18) to obtain eight linear algebraic homogeneous equations, which are used to determine the eight unknown constants B_i, D_i (i = 1, 2, 3) and A_2, C_2. The determinant of the matrix M should be zero for non trivial solutions B_i, D_i (i = 1, 2, 3) and A_2, C_2. Once the critical stress and its corresponding buckling wavelength are found, the constants B_i, D_i (i = 1, 2, 3) and A_2, C_2 can be determined up to an arbitrary constant. The matrix M is

$$
M = \begin{bmatrix}
-n_1 & -n_2 & 0 & k_1 n_1 & k_2 n_3 & 0 & c_2 & -k_2 c_3 \\
-m_1 c_1 & -c_2 & 0 & c_1 & -c_3 & 0 & n_2 & n_3 \\
t_1 c_1 & 2G_2 c_2 & 0 & t_2 c_1 & t_5 c_3 & 0 & -2G_2 n_2 & -t_5 n_3 \\
t_3 n_1 & 2G_2 n_2 & 0 & t_4 n_4 & t_6 n_3 & 0 & -2G_2 c_2 & -t_6 c_3 \\
0 & -n_2 & -1 & 0 & k_2 n_3 & k_3 & -c_2 & k_2 c_3 \\
0 & c_2 & -1 & 0 & c_3 & -1 & n_2 & n_3 \\
0 & -2G_2 c_2 & 2G_3 & 0 & -t_5 c_3 & t_8 & -2G_2 n_2 & -t_5 n_3 \\
0 & 2G_2 n_2 & 2G_3 & 0 & t_6 n_3 & t_6 & 2G_2 c_2 & t_6 c_3
\end{bmatrix}
\tag{2.19}
$$

where n_i (i = 1,2,3,4) and t_j (j = 1,2,3,...,8) are defined as follows

$$
\begin{aligned}
&n_1 = sinh(\beta_1 h_1), && c_1 = cosh(\beta_1 h_1)\\
&n_2 = sinh(h_2), && c_2 = cosh(h_2)\\
&n_3 = sinh(\mu_2 h_2), && c_3 = cosh(\mu_2 h_2)\\
&n_4 = sinh(\mu_1 h_1), && t_1 = G_{12}(-m_1 - \beta_1)\\
&t_2 = G_{12}(k_1\mu_1 - 1), && t_5 = G_2(1 - k_2\mu_2)\\
&t_3 = \tfrac{-(1+\upsilon_{23})\upsilon_{21}E_1 + (1-\upsilon_{21}\upsilon_{12})E_2 m_1 \beta_1}{\Delta}, &&\\
&t_4 = \tfrac{(1+\upsilon_{23})\upsilon_{21}E_1 k_1 + (1-\upsilon_{21}\upsilon_{12})E_2 \beta_1}{\Delta}, &&\\
&t_6 = \lambda_2 k_2 + \lambda_2 \mu_2 + 2G_2\mu_2, &&\\
&t_7 = G_2(k_2\mu_2 - 1), && t_8 = -G_3(k_3\mu_3 - 1)
\end{aligned}
\tag{2.20}
$$

Here $h_1 = \alpha D/2$, $h_2 = \alpha t/2$.

2.3 Finite Element Verification of Model Prediction

In the analytical model for the analysis to determine the onset of buckling of fiber, the matrix is assumed to be infinitely thick. Without loss of generality and considering limitations on computational resources for the finite element model, matrix thickness is set to be 50 times of the thickness of fiber, and periodic boundary condition is defined on two vertical edges. Numerical analysis is performed in the commercial finite element software package ABAQUS 6.14 to validate the theoretical approach of determining the critical stress and its buckling behavior. The fiber is modeled as transversely isotropic elastic material and the following parameters are used: $E_{fx_1} = 276GPa$, $E_{fy_1} = 19.5GPa$, $G_{x_1y_1} = 70GPa$, $\upsilon_{x_1y_1} = 0.28$, $\upsilon_{y_1z_1} = 0.7$ (Upadhyaya et al., 2013). The interphase region and matrix are modeled as isotropic elastic material. It is assumed that the interphase region properties change with the volume fraction of MWNT sheets in the matrix, the interphase region's Young's modulus increase as the volume fraction of MWNT sheets increases and Poisson's ratio changes as well

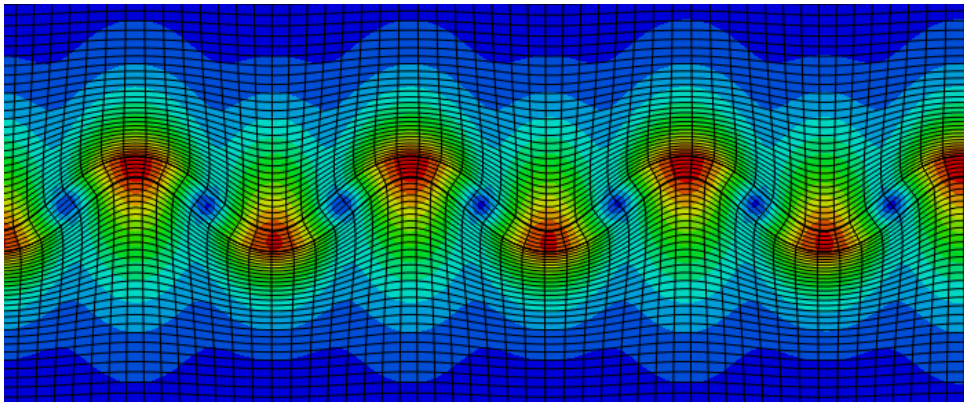

Figure 2.11: Anti-symmetric buckling mode obtained from linear buckling analysis.

(Tsuda et al., 2014). Eight-node quadratic plane strain elements are used for fiber, interphase region and matrix. There are 1000 elements along the fiber direction, resulting in very small characteristic element lengths compared with buckling wavelength. In order to guarantee the accuracy of buckling strain, there are more than one element along the thickness direction of fiber and interphase region, and mesh convergence studies were conducted to ensure that mesh independence was achieved. Antisymmetric buckling modes observed from the finite-element analysis using linear buckling method are shown in Figure 2.11, which validates the assumption of antisymmetric buckling models assumed in the theoretical model development.

2.4 Results and Discussion

Parametric analysis was conducted using our analytical model predictions as well as FEA to examine role of the thickness of the interphase region on the mechanical properties, and compressive strain at the onset of buckling. Notice that the solid lines represent theoretical result, and scatter symbols represent FEA simulation results in Figures 2.12-2.16. It is observed that different buckling strain as a function of buckle half wavelength (0.5 λ_w/D) curves obtained by treating fiber as anisotropic and isotropic are quite different, as shown

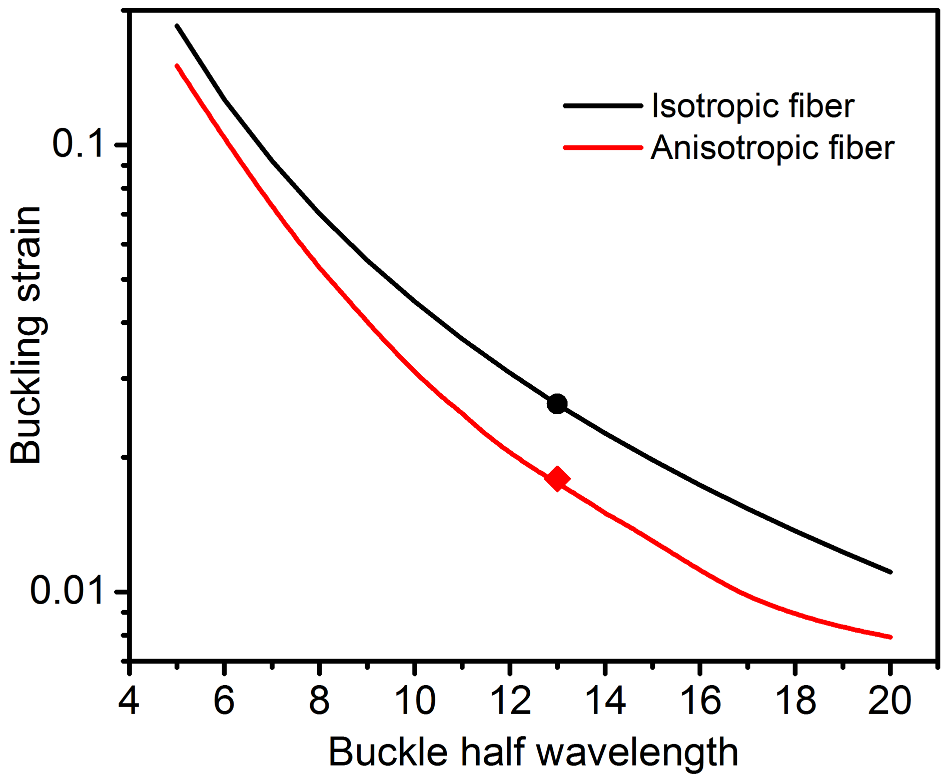

Figure 2.12: Comparison of buckling strain (logarithmic scale) for the unidirectional composites for two situation where a carbon fiber is modeled as an anisotropic and an isotropic material. In both anisotropic and isotropic models, the carbon fiber longitudinal modulus is set equal. It is seen that assuming isotropic behavior for a carbon fiber over-estimates the critical strain at buckling.

in Figure 2.12. It can be seen that for a fixed buckle half wavelength, buckling strain determined by modeling the fiber as anisotropic is significantly lower than that determined by modeling fiber as isotropic. Figure 2.12 show that the ratio of isotropic model to anisotropic model buckling strain reaches a maximum 1.58 for buckle half wavelength equaling 16. The parameters used to determine buckling strain and buckle half wavelength are: Young's modulus of matrix E_m is 3.5 GPa, Poisson's ratio of matrix υ_m is 0.38, and Young's modulus of interphase region E_i is 20 GPa, Poisson's ratio of interphase region υ_i is 0.33, and $t/D = 0.07$. The effect of interphase region thickness was studied by changing the ratio of the thickness of the interphase region with respect to the fiber's thickness. Theoretical critical strain shows

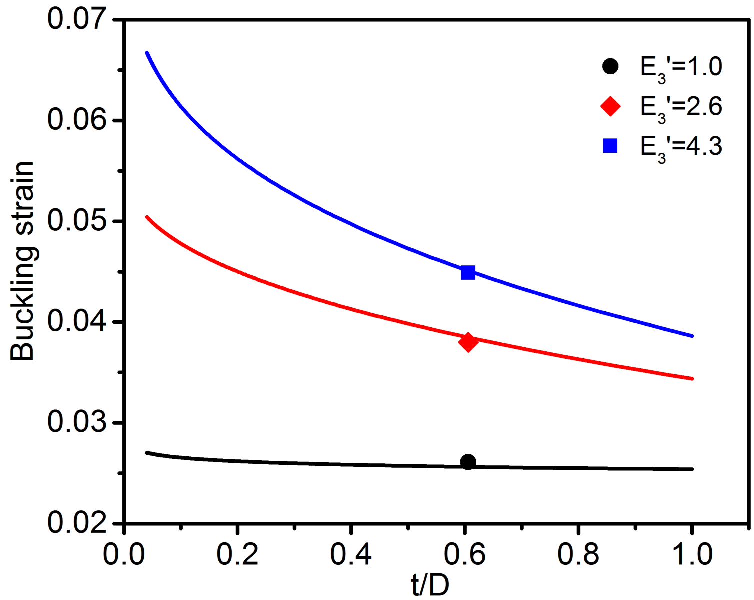

(a)

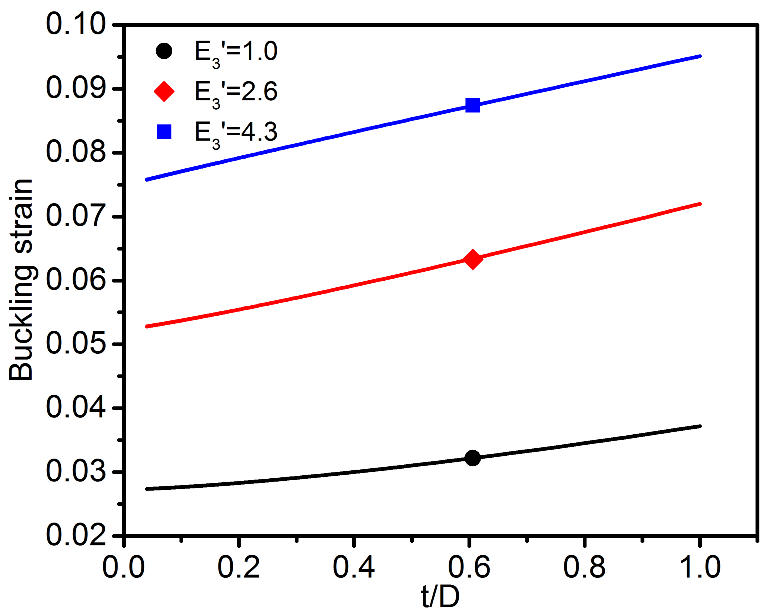

(b)

Figure 2.13: Simulation and theoretical analysis are carried on at the same situation for both cases except interphase region Young's modulus. Solid lines are theoretical results and symbols are FEM results. (a) Variation of buckling strain against t/D for 'soft' interphase region ($E_i < E_m$). (b) Variation of buckling strain against t/D for 'stiff' interphase ($E_i > E_m$). Here $E_{m0} = 3.5GPa$, $E_3' = E_m/E_{m0}$.

a good agreement with the numerical result for different thickness ratio as shown in Figures 2.13a and 2.13b. It should be noted that the maximum ratio of interphase region thickness to fiber diameter is set at 1, assuring that fiber's property dominates in the composites and the diameter of the fiber $D = 5\mu m$ is fixed. In Figure 2.13a, when the thickness ratio increases, buckling strain decreases in the case where interphase region modulus 2.5 GPa is less than matrix modulus (i.e., a 'soft' interphase region). It means that soft' interphase region could not provide strong support for carbon fiber under compression, making it easier to buckle. It is noted that buckling strain increases with the increase of matrix modulus in Figure 2.13a, the more strong the matrix is, the more support can give to carbon fiber making it not easy to buckle under compression. However a reversed trend is observed in the case where interphase region modulus 25 GPa is larger than matrix modulus ('stiff' interphase region) in Figure 2.13b. Figure 2.13b shows that wrapping MWNTs on carbon fiber helps increase the buckling strain, which increase linearly with the interphase region thickness. The buckling strain can increase by 35.9%, 36.3%, 25.5% when interphase region thickness equals fiber diameter for $E_3' = 1.0$, $E_3' = 2.6$, $E_3' = 4.3$, respectively, compared with baseline datas when no interphase region in such composite. The higher matrix Young's modulus can help improve the buckling strain no matter what the interphase region property is, both as shown in Figures 2.13a and 2.13b. It is seen that a thick interphase region (bigger t/D) can induce larger wavelength for 'soft'and 'stiff' interphase region in Figure 2.14 and Figure 2.15, from which we can observe that buckle half wavelength decreases as matrix's Young's modulus increases. Figure 2.16 shows the curves for the critical strain with respect to Young's modulus ratio of interphase region to matrix from theoretical analysis and finite element simulation. It illustrates that E_i/E_m almost does not affect buckle strain when the interphase region thickness is very small. When interphase region thickness is comparable with fiber's diameter, buckling strain increases with interphase Young's modulus initially and it does not change much subsequently. Notice that there is an optimal interphase region

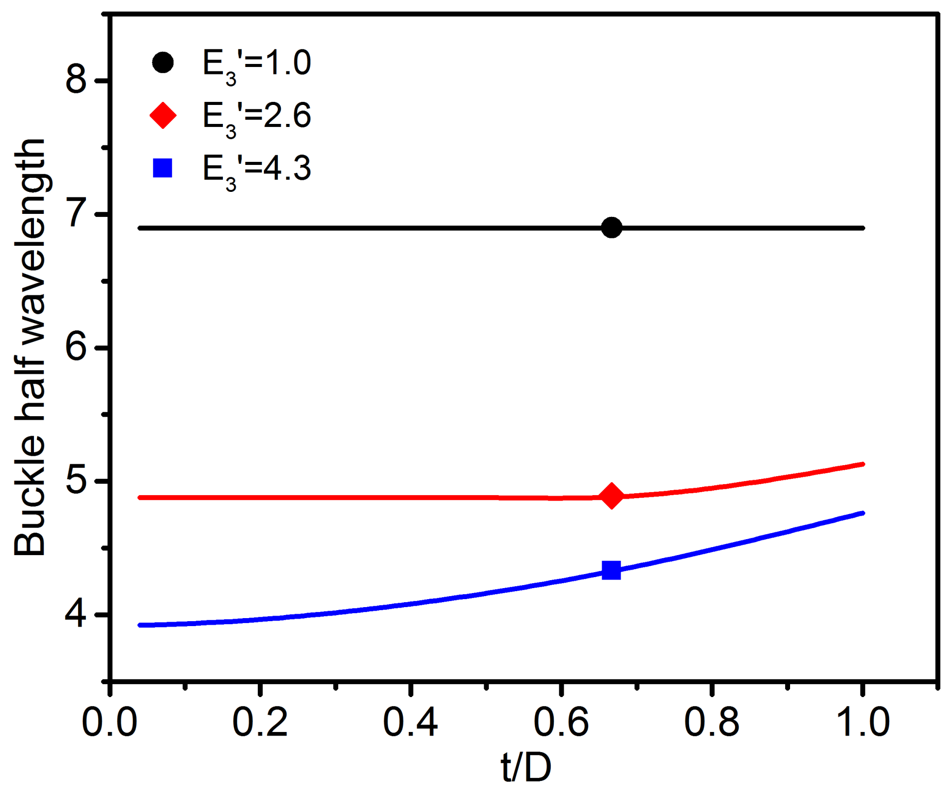

Figure 2.14: Variation of buckle half wavelength against t/D for 'soft' interphase region ($E_i < E_m$). Solid lines are theoretical results and symbols are FEM results.

Young's modulus around 17.5 GPa for such composite, which can be achieved by controlling volume fraction of MWNTs and epoxy, and wrapping bias angle.

2.5 Summary and Conclusions

A theoretical model for studying the compressive buckling strain of a unidirectional carbon-fiber/epoxy composite was presented. In the model, the composite is considered to consist of three constituents: fiber, nanocomposite (CNT/matrix interphase region), and matrix. The fiber, nanocomposite and matrix (e.g., epoxy) are modeled as a transversely isotropic, and isotropic elastic continuum respectively. The analysis is conducted under a plain strain condition applying a small perturbation in the field equations. Perfect bonding is assumed at the fiber/ nanocomposite interface, and nanocomposite/matrix interface to make sure

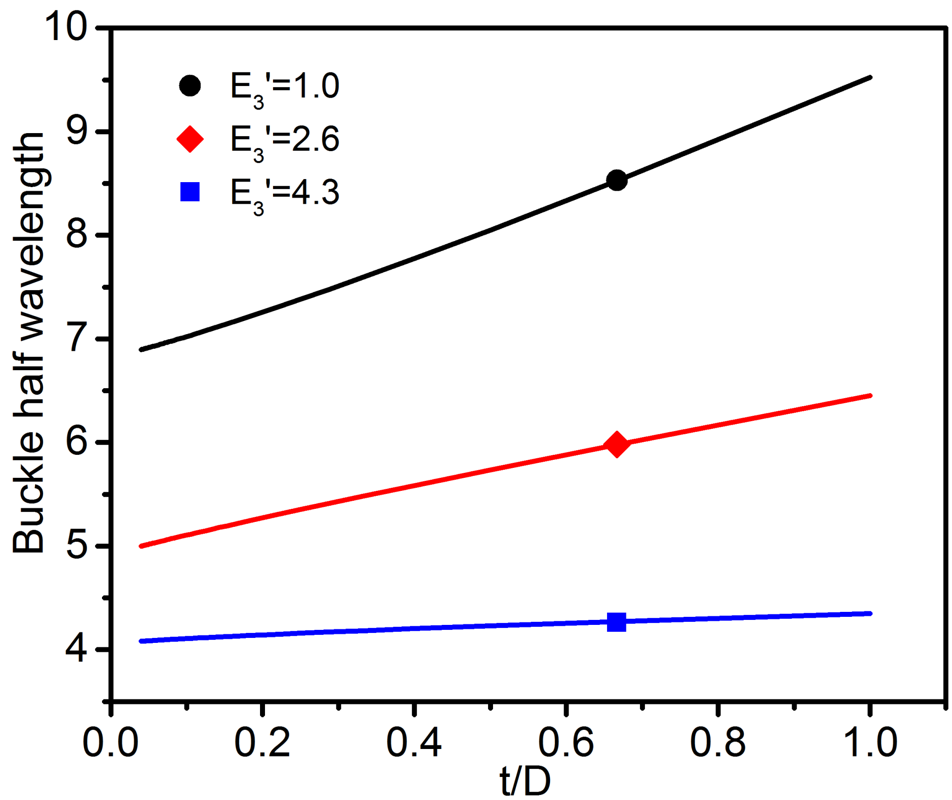

Figure 2.15: Variation of buckle half wavelength against t/D for 'stiff' interphase ($E_i > E_m$). Here $E_{m0} = 3.5\ GPa$, $E_3' = E_m/E_{m0}$. Solid lines are theoretical results and symbols are FEM results.

displacement and traction are continuous at the interface. Buckling strain and corresponding wavelength for antisymmetric deformation mode are obtained from the analysis. Finally, comparing buckling strain determined by modeling fiber as anisotropic with modeling fiber as isotropic, the current model predicts lower buckling strain. FEM simulations were carried out to simulate the same buckling problem for model verification, and it shows consistent results with theoretical analysis. The effects of the nanocomposite's thickness, Young's modulus of interphase region and matrix on buckling strain and wavelengths were discussed. Wrapping CNT sheet on carbon fiber indeed helps improve compressive strength as long as nanocomposite's Young's modulus is higher than the matrix, which is easily achievable by controlling volume fraction of MWNT and wrapping bias angle. The optimum interphase region thick-

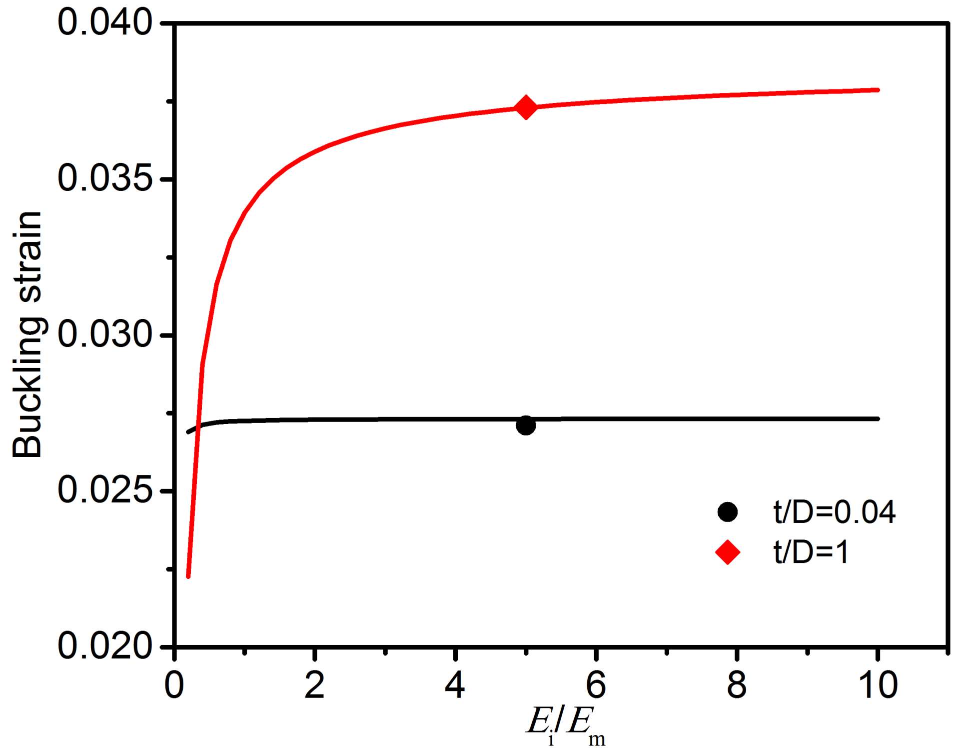

Figure 2.16: Variation of buckling strain against Young's modulus ratio of interphase region to matrix using $\upsilon_m = 0.38$ and $\upsilon_i = 0.2$. Solid lines are theoretical results and symbols are FEM results.

ness is fiber's diameter under the assumption that fiber's property dominates composites. In summary, the theoretical analysis here provides a potentially powerful method for designing composite components through analyzing the compressive behavior of composites with transversely isotropic fibers and tailored interphase stiffness.

CHAPTER 3

THEORY FOR POLYMER COATED CNT YARN ARTIFICIAL MUSCLE DRIVEN BY VAPOR

3.1 Prediction of the Effect of Polymer/Core Ratio on the Absorption-driven Torsional Actuation of a Polymer Coated CNT Yarn

Corresponding to the method presently used to make a twisted polymer coated CNT yarn artificial muscles, this theoretical analysis considers a polymer coated CNT yarn artificial muscle core yarn having an initial twist of T_0 (turns per muscle length), which is clamped and coated with the polymer material until the polymer dries to set the initial state of the polymer coated CNT yarn artificial muscle. If the yarn was unclamped before the polymer was applied, then the yarn will decrease twist by ΔT_0 due to elastic removal of most of the inserted twist. The fully dried polymer coated CNT yarn artificial muscle is unclamped at one end allowing rotation that removes a twist of ΔT_{off} from the core yarn, and introduces twist into the polymer coated CNT yarn artificial muscle's polymer. In the equilibrium non-actuated state, the torque on the CNT core is balanced by the opposing torque in the elastically twisted polymer, so that:

$$0 = k_{core}^{off}(\Delta T_0 + \Delta T_{free,off} - \Delta T_{off}) - k_{polymer}^{off}\Delta T_{off} \tag{3.1}$$

where k_{core} and $k_{polymer}$ are the torsional stiffnesses of the core and polymer sheath, respectively, and $\Delta T_{free,off}$ is the change in core twist due solely to the compression applied by the drying polymer. Rearranging Equation (3.1) gives:

$$\Delta T_{off} = \frac{\Delta T_0 + \Delta T_{free,off}}{1 + \frac{k_{polymer}^{off}}{k_{core}^{off}}} \tag{3.2}$$

Using the above approach, we can now calculate the twist change (ΔT_{on}) in going from initial yarn twist (T_0) to the twist that results from actuation of the polymer coated CNT yarn artificial muscle. Now the torque balance equation is written as:

$$0 = k_{core}^{on}(\Delta T_0 + \Delta T_{free,on} - \Delta T_{on}) - k_{polymer}^{on}\Delta T_{on} \tag{3.3}$$

Hence,

$$\Delta T_{on} = \frac{\Delta T_0 + \Delta T_{free,on}}{1 + \frac{k_{polymer}^{on}}{k_{core}^{on}}} \tag{3.4}$$

The torsional stroke of the polymer coated CNT yarn artificial muscle (in turns per muscle length) is:

$$\Delta T_{PCAM} = \Delta T_{on} - \Delta T_{off} \tag{3.5}$$

Since the modulus of the yarn in the axial direction is much lower than that in radial directions, we can approximate that the length of the polymer coated CNT yarn artificial muscle does not change during torsional actuation. This approximation is supported by experiment result that this tensile stroke is a 1.25% contraction. On the other hand, the polymer coated CNT yarn artificial muscle's diameter increases by 9% during this actuation.

Hence, we approximate that the change in twist of the yarn core occurs without energetically costly changes in nanotube length (which is the string length in the helix model) or polymer coated CNT yarn artificial muscle length. Correspondingly, the helix equation (I) gives that the fractional change in twist equals the fractional change of the diameter of the core yarn. Consequentially, we obtained that:

$$\Delta T_{free,on} = \frac{T_0 + \Delta T_0}{\frac{d_{core}^{Uncoated}}{d_{core}^{on}} - 1} \tag{3.6}$$

$$\Delta T_{free,off} = \frac{T_0 + \Delta T_0}{\frac{d_{core}^{Uncoated}}{d_{core}^{off}} - 1} \tag{3.7}$$

where d_{core} parameters are the yarn core diameters in the uncoated ($d_{core}^{Uncoated}$), actuation-off (d_{core}^{off}), and actuation-on (d_{core}^{on}) states.

The core diameter of the polymer coated CNT yarn artificial muscle after drying in the non-actuated state (d_{core}^{off}) is estimated by first considering the compression ratio $\lambda =$

$d_{core}^{on}/d_{core}^{off}$. This compression ratio, which is a function of the polymer sheath/core ratio (SCR), can be evaluated from elasticity theory by drawing analogy to the case where a core cylinder is inserted into a hollow tube that has an initial inner radius that is smaller than the initial radius of the core cylinder. Using literature results (Shigley, 2011), λ is obtained from:

$$\lambda = 1 - \frac{1-\phi}{\lambda_t + \lambda} \tag{3.8}$$

where λ_t is defined:

$$\lambda_t = \frac{\lambda E_c}{E_s(1-\nu_s)}\left(\frac{(1+2x/\lambda)^2+1}{(1+2x/\lambda)^2-1} + \nu_s\right) \tag{3.9}$$

where ϕ is the ratio of the polymer thickness in the non-actuated state to the polymer thickness in the actuated state. E_s and E_c are the elastic moduli of the polymer and the core, respectively, in the radial direction, and ν_s and ν_c are the corresponding Poisson's ratios that couple a stretch in the circumferential direction to the deformation in the radial direction.

We will now apply these theoretical results for the specific case of predicting the dependence of torsional actuation on polymer/core ratio for ethanol-driven actuation of a polymer@CNT polymer artificial muscle. Since experimental measurements show that the Young's modulus for the polymer of the ethanol-saturated polymer coated CNT yarn artificial muscle is very low (50.4 MPa) compared to fiber modulus in the yarn direction, the elongation of twisted polymer coated CNT yarn artificial muscle during actuation can be neglected. Since stresses on the polymer coated CNT yarn artificial muscle core are similar for the actuated state and the initial non-coated state, we approximate that $d_{core}^{Uncoated} = d_{core}^{on}$. For calculating the torsional stroke as a function of polymer/core ratio, we input the geometry of the non-actuated polymer coated CNT yarn artificial muscle, the elastic properties of both the sheath and core, and the percent volume change of the sheath material during ethanol absorption. The elastic modulus of the core yarn in the radial direction was obtained by mechanically loading the torsional polymer coated CNT yarn artificial muscle with tensile stress provided by the rotor used for torsional measurements, and then compressing the yarn in the radial direction while stress-strain measurement were obtained. After correcting for the circular shape of the yarn using a conventionally applied equation (Puttock and Thwaite, 1969), 65.9 MPa was obtained for the radial-direction Young's modulus. Insert how Poisson's ratio was obtained. The Young's modulus of the sheath, in pristine and ethanol-saturated states (294 MPa and 50.4 MPa, respectively), was derived from tensile stress-strain measurement on a rectangular strip of the sheath material.

Equations (3.5)-(3.8) were solved, using the above obtained values of the Young's modulus and the Poisson's ratio of sheath and core in the non-actuated state, and the shear modulus of the sheath and core. The shear modulus of the sheath material was obtain from the relationship between Young's modulus and shear modulus for an isotropic material (105 MPa). The shear modulus of the twisted yarn core (150 MPa) was derived from the observed rate of yarn untwist to rotate a paddle of known moment of inertia. The relationship between shear modulus (G) and torsional stiffness (k) for a rod of length (L) and cross-sectional polar 2^{nd} moment of area (J), which is $k = GJ/L$, is here exploited. The diameter of core of the polymer coated CNT yarn artificial muscle is 35.0 μm, and the thickness of sheath can be calculated from the SCR and the diameter of the core. For the polymer infiltrated CNT yarn artificial muscle, the host and guest co-share the same yarn volume and the yarn diameter is 44.2 μm. The length of the polymer coated CNT yarn artificial muscle and polymer infiltrated CNT yarn artificial muscle are both 48.0 mm.

Calculation of the torsional stiffness for the polymer infiltrated CNT yarn artificial muscle proceeds analogously, except that the rule-of-mixtures is used to calculate the effective shear modulus of the polymer infiltrated CNT yarn artificial muscle.

Using these experimental measurements of polymer and core properties, and the approximation that $d_{core}^{Uncoated} = d_{core}^{on}$ (and using no fit parameters), predicted dependence of torsional

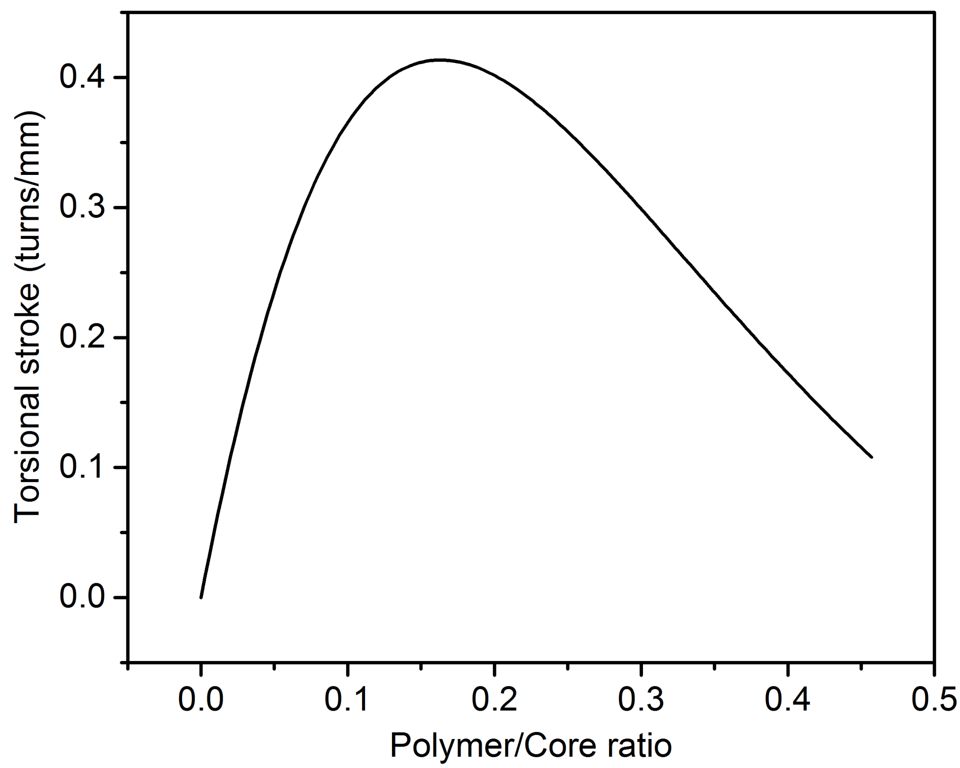

Figure 3.1: The predicted dependence of torsional stroke on polymer thickness to core diameter ratio (polymer/core ratio) for twisted Polymer@CNT artificial muscles .

actuation on the polymer/core ratio Figure 3.1. It can be seen that the theory predicts zero torsional stroke when the polymer/core ratio is either zero or infinite. In addition, there is an optimum value of the polymer/core ratio for maximizing torsional stroke.

3.2 Predicted Tensile Stroke and Isobaric Contractile Work Capacity of Coiled Polymer Coated CNT Yarn Artificial Muscles and Polymer Infiltrated CNT Yarn Artificial Muscles

While the calculations in this section pertain to any means of driving actuation, we here focus discussion on the specific case where actuation results from vapor or liquid absorption and desorption. Hence, mechanical parameters have subscripts "dry" or "wet" depending upon whether they pertain to the non-actuated or actuated states. The dependence of

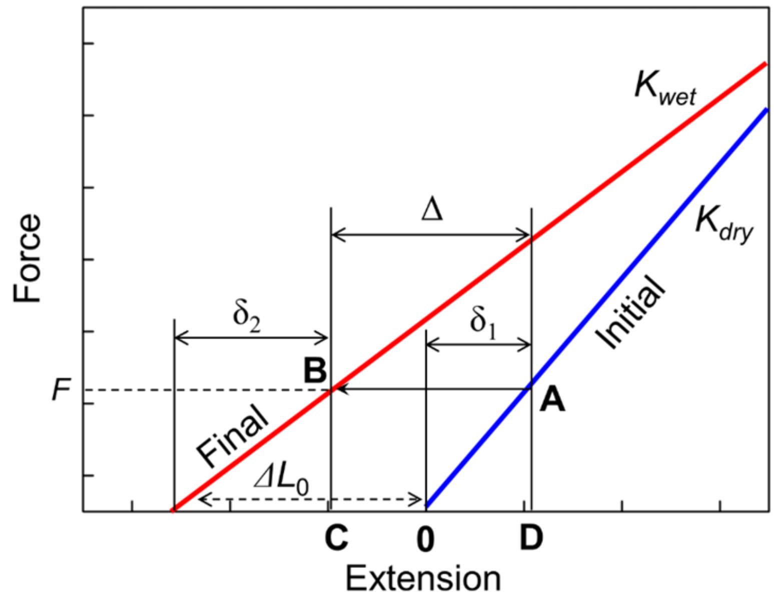

Figure 3.2: Schematic illustration of the force-extension dependence for actuated and non-actuated coils, which is used for the calculation of contractile work capacity. This calculation uses the approximation that the stiffness of the muscle coil is strain independent for both non-actuated (dry) and actuated (wet) states. The symbols in this illustration are defined in this section.

muscle stroke (ΔL) and contractile work capacity (W) on isobaric load (F) were calculated for both polymer coated CNT yarn artificial muscles and polymer infiltrated CNT yarn artificial muscles from the force-extension curves shown in Figure 3.2, which approximate that the helical springs in non-actuated and actuated states have strain-independent spring stiffnesses, K_{dry} and K_{wet}, respectively. The isobaric tensile stroke becomes

$$\Delta L = \delta_1 + \Delta L_0 - \delta_2 = \Delta L_0 - (\frac{F}{K_{wet}} - \frac{F}{K_{dry}}) \tag{3.10}$$

where $\delta_1 = \frac{F}{K_{dry}}$ and $\delta_1 = \frac{F}{K_{wet}}$. ΔL_0 is defined as the free tensile stroke, which is the stroke that would arise for a vanishing load if inter-coil contact did not occur. This free stroke would also be the observed stroke if the spring stiffnesses for the muscle were the same in the actuated and non-actuated states. When actuation takes place under isotonic loading, the area enclosed by the rectangle ABCD provides the contractile work capacity, which is:

$$W = F\Delta L = F(\delta_1 + \Delta L_0 - \delta_2) = F\Delta L_0 - (\frac{F^2}{K_{wet}} - \frac{F^2}{K_{dry}}) \tag{3.11}$$

Equations (3.10) and (3.11) show that isobaric tensile stroke and contractile work capacity are determined by both the free stroke (ΔL_0) and the stiffness change ($1/K_{wet} - 1/K_{dry}$). However, the two terms provide opposite effects: contractile stroke ΔL_0 is produced when the muscle volume expands during activation to produce muscle untwist, while the stiffness change (from non-activated to activated state) leads to an extension of the spring when $K_{wet} < K_{dry}$, which is usually the case.

In order to complete the calculations, we next derive the free stroke ΔL_0. Based on the twist-driven coil actuation mechanism, the free stroke is $\Delta L_0 = \frac{l^2 \Delta T}{N}$, where l is the fiber length, ΔT is the fiber untwist (torsional actuation) due to guest volume expansion and modulus decrease, and N is the number of coils in the fiber length.

Using a theoretical framework that is similar to the one used for non-coiled muscles, the torsional actuation stroke ΔT can be estimated as follows: In the case of a coiled polymer coated CNT yarn artificial muscle, the torque on the CNT core is balanced by the external torque (TQ) needed to provide torsional tethering. In the non-actuated state,

$$TQ = k_{core}^{off}(\Delta T_0 + \Delta T_{free,off}) \tag{3.12}$$

where k_{core}^{off} is the torsional stiffness of the core in the non-actuated state, and $\Delta T_{free,off}$ is the change in core twist due solely to the compression applied by the drying polymer. The torque balance equation in the actuated state is written as:

$$TQ = k_{core}^{on}(\Delta T_0 + \Delta_{free,on} - \Delta T) - k_{polymer}^{on}\Delta T \tag{3.13}$$

Combining Equations (3.12) and (3.13) gives

$$k_{core}^{off}(\Delta T_0 + \Delta T_{free,off}) = k_{core}^{on}(\Delta T_0 + \Delta T_{free,on} - \Delta T) - k_{polymer}^{on}\Delta T \tag{3.14}$$

which provides the following for the torsional stroke of the polymer coated CNT yarn artificial muscle (in turns per muscle length):

$$\Delta T = \frac{k_{core}^{off}(\Delta T_0 + \Delta T_{free,off}) + k_{core}^{on}(\Delta T_0 + \Delta T_{free,on})}{k_{core}^{on} + k_{polymer}^{on}} \tag{3.15}$$

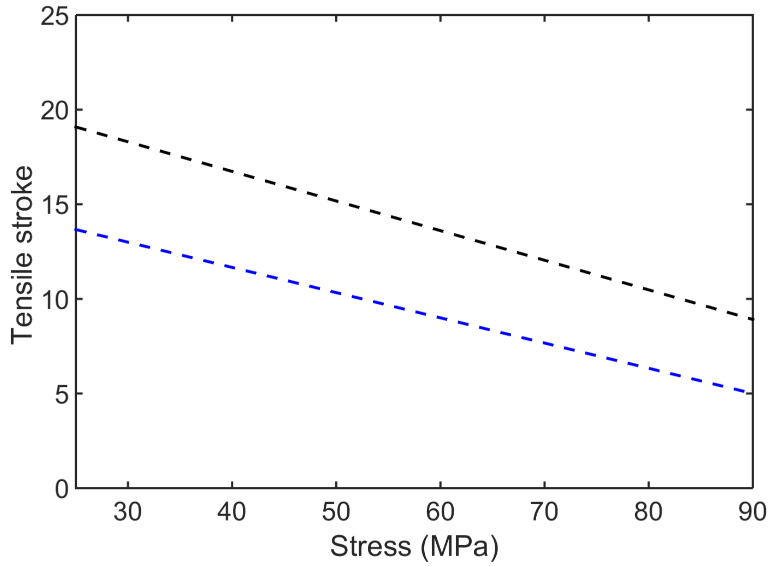

Figure 3.3: Comparison of the stress dependence of theoretically calculated tensile stroke (% of non-loaded length) for a polymer coated CNT yarn artificial muscle (dashed black line) and a polymer infiltrated CNT yarn artificial muscle (dashed blue line).

Using an essentially identical approach, the torsional stroke for the polymer infiltrated CNT yarn artificial muscle is:

$$\Delta T = \frac{k_{host}^{off}(\Delta T_0 + \Delta T_{free,off}) + k_{host}^{on}(\Delta T_0 + \Delta T_{free,on})}{k_{host}^{on} + k_{guest}^{on}} \tag{3.16}$$

where k_{host}^{off} and k_{host}^{on} are the torsional stiffnesses of the host in the non-actuated and actuated state, respectively.

These calculations of torsional stroke for a coiled Polymer@CNT artificial muscle and coiled polymer infiltrated artificial muscle use the same torsional stiffnesses as used for predicting the torsional stroke of a twisted polymer coated CNT yarn artificial muscle and a twisted polymer infiltrated artificial muscle in Section 3.1. The resulting ΔT is 0.17 turns/mm for the coiled polymer coated CNT yarn artificial muscle and 0.11 turns/mm for the coiled polymer infiltrated artificial muscle.

We next predict the free tensile stroke (ΔL_0) for a vapor-driven coiled polymer@CNT artificial muscle and for an ethanol-vapor-driven coiled polymer infiltrated CNT yarn artificial

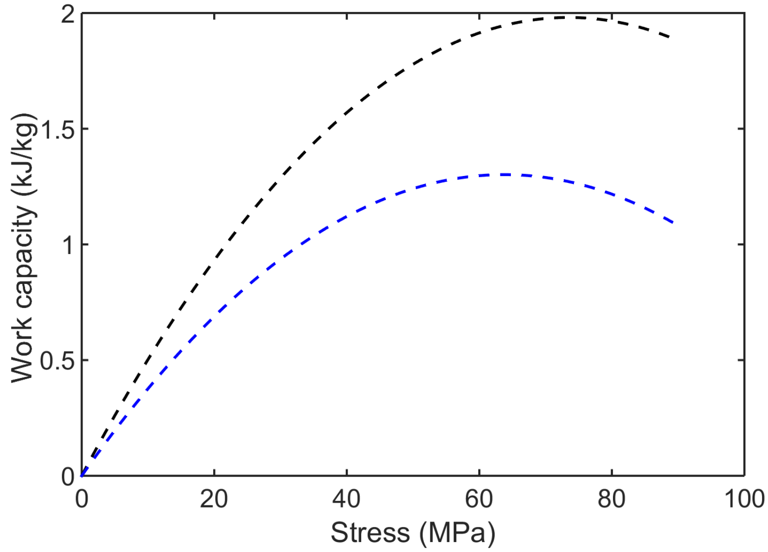

Figure 3.4: Comparison of the stress dependence of theoretically calculated work capacity for a polymer coated CNT yarn artificial muscle (dashed black line) and a polymer infiltrated CNT yarn artificial muscle (dashed blue line).

muscle using the relationship that $\Delta L_0 = \frac{l^2 \Delta T}{N}$. For the investigated muscles, the number of coils (N) in the polymer coated CNT yarn artificial muscle and in the polymer infiltrated CNT yarn artificial muscle were $N = 106$ and $N = 116$, respectively and the fiber length within the coiled polymer coated CNT yarn artificial muscle and polymer infiltrated CNT yarn artificial muscle were $l = 5.6$ cm and $l = 5.8$ cm, respectively. Using the ΔT values predicted using Equations (3.15) and (3.16) (0.17 and 0.11 turns/mm for the polymer coated CNT yarn artificial muscle and polymer infiltrated CNT yarn artificial muscle, respectively), ΔL_0 becomes 5.1 mm and 3.1 mm for the polymer coated CNT yarn artificial muscle and polymer infiltrated CNT yarn artificial muscle, respectively. resulting ΔT is 0.17 turns/mm for the coiled polymer coated CNT yarn artificial muscle and 0.11 turns/mm for the coiled polymer infiltrated artificial muscle.

Using Equations (3.10) and (3.11), respectively, and the above values of ΔL_0, provides the predicted dependence of tensile stroke and contractile work capacity on the applied isobaric stress. As shown in Figure 3.3 and Figure 3.4, respectively, the theoretically tensile stroke and work capacities of polymer coated CNT yarn artificial muscle are higher than those of polymer infiltrated CNT yarn artificial muscle for stress levels that are sufficiently high that coil-coil contact does not limit actuation.

CHAPTER 4

ANALYTICAL MODEL AND OPTIMIZATION OF ENERGY HARVESTING USING TORSIONAL NYLON ARTIFICIAL MUSCLE

4.1 Introduction

Recently, many researches focus on designing a low-cost and high-performance device to extract (harvest) energy from the environment, to either recharge a secondary battery or, to power directly the electronics. For example, the lifespan of wireless sensor networks can be affected by the battery, if we can use some device to recharge the battery, which can prolong the lifespan of such system (Tutuncuoglu and Yener, 2012; Ottman et al., 2002, 2003); another application is in wearable electronics, where energy harvesting devices can power or recharge cellphones, mobile computers, radio communication equipment, etc (Mitcheson et al., 2008; Beeby et al., 2006; Khaligh et al., 2010). Transduction mechanism required by energy harvesting generates electrical energy from motion and transduction mechanism consists of piezoelectric, electromagnetic and electrostatic. Active materials employed in piezoelectric generators generate a charge when mechanically stressed. Piezoelectric generators (Fang et al., 2006; Cook-Chennault et al., 2008) include impact coupled, resonant and human-based devices. Electromagnetic induction employed by electromagnetic generators (Beeby et al., 2007; Cao et al., 2007) arises from the relative motion between a magnetic flux gradient and a conductor. A comprehensive review of existing electromagnetic generators is presented, including large scale discrete devices and wafer-scale integrated versions. Relative movement between electrically isolated charged capacitor plates is used by electrostatic generators (Liu et al., 2005; Paracha et al., 2006) to generate energy. The harvested energy is provided by the work done against the electrostatic force between the plates. Electrostatic-based generators are reviewed under the classifications of in-plane overlap varying, in-plane gap closing and out-of-plane gap closing; the Coulomb force parametric generator and electret-based generators are also covered.

For this paper, the new design works the same with electromagnetic generators, however, the rotation of magnet is due to rotation of torsional artificial muscle (nylon spring). Baughman (Haines et al., 2014) showed that inexpensive high-strength polymer fibers can be easily transformed by twist insertion to provide fast, scalable, non-hysteretic, long-life tensile and torsional muscles. Extreme twisting produces coiled muscles that can generate 5.3 kilowatts of mechanical work per kilogram of muscle weight, similar to that produced by a jet engine. Baughman (Mirvakili et al., 2014) showed that helical springs can be formed by twisting and then coiling monofilaments nylon and polyethylene fibers. Such helical springs twisted and untwisted due to the change of temperature was used in this paper to make sure the rotation of magnet.

Researchers have been proposed many integrated micro power supplies recently. Energy coupling method to remotely induce voltages on-chip by magnetic field was proposed by Matsuki et al. in 1988 (Matsuki et al., 1988). Rechargeable lithium micro batteries which were used as self-contained on-board power supply was developed by Bate et al. in 1993 (Bates et al., 1993). A miniaturized high-voltage solar cell array which was effective in driving electrostatic silicon mirrors was built by Lee et al. in 1995 (Lee et al., 1995). Koeneman et al. presented a comprehensive study on the feasibility of micro power supplies for MEMS in 1997 (Koeneman et al., 1997). An electromagnetic micro generator that attached a magnet to a flexible polyimide membrane to produce 0.3 μW on a planar pick-up coil was developed by Shearwood and Yates (Williams et al., 2001) and Williams and Yates (Williams and Yates, 1996) in 1997. A signal processing circuitry was driven by a macro (500mg mass, with conventional springs) vibration-based power generator, which was successful invented by Amirtharajah and Chandrakasan (Amirtharajah and Chandrakasan, 1998) in 1998. Neil et al. designed printed circuit board integrated vibration-induced power generator. They built a mechanically based integrated MEMS power generator which will convert vibrational kinetic energy transferred from the immediate environment to electrical energy usable by a low-power CMOS circuit chip and integrated micro-sensors in 2000 (Ching et al., 2000). Nakano

(Okazaki et al., 2002) designed a portable generator using vibration due to human walking in 2002. Dennis (Hohlfeld et al., 2008) proposed and demonstrated an electromagnetic energy scavenging scheme which can harvest energy from non-harmonic motion in 2008. In this paper, based on artificial muscle, electromagnetic generator was designed. Artificial muscle will twist and untwist due to the change of temperature, resulting in the magnet to rotate because the interaction between nylon and magnets. Voltage and current will be induced in coil since the rotation of magnet. In order to make sure transfer efficiency from kinetic energy to electrical energy high, mathematical model was built to study the best combination of parameters using optimization method (Duan et al., 1994).

4.2 A Coupled Mechanical-Electrical Model

Researchers (Kim et al., 2015) used nylon 6 fibers deployed for fishing lines to fabricate torsional muscles. First, they fixed one end of nylon fiber to the shaft of stepper motor to insert twist, and the other end was attached to a weight to prevent from rotating. The

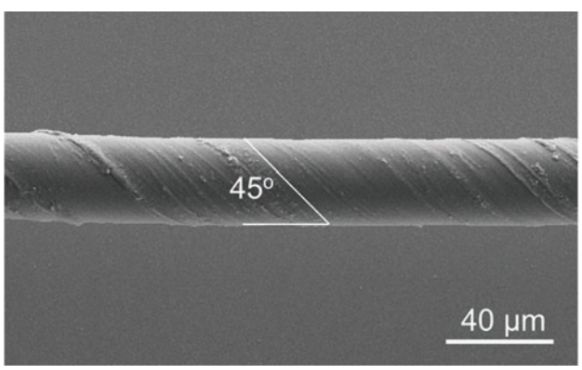

(a)

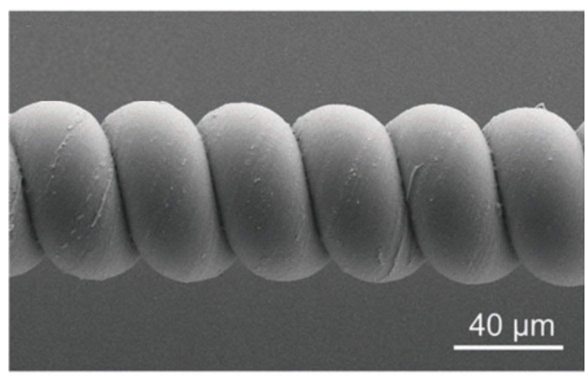

(b)

Figure 4.1: (a) Twisted nylon fiber (Kim et al., 2015). (b) Coiled nylon fiber (Kim et al., 2015).

twisted nylon fiber can be seen in Figure 4.1a. Coiled muscle is formed by further inserting twist until complete coiling occurred, and at the same time the fiber was treated by heat under vacuum at 210°C for 2 hours. Figure 4.1b shows the coiled artificial muscle. Different configuration of artificial muscle for energy harvesting are shown in Figure 4.2a and Figure 4.2b. As shown in Figure 4.2a, only one segment of such setup is heated, resulting in untwist of this segment and up-twist of the other unheated segment. As Figure 4.2a shows

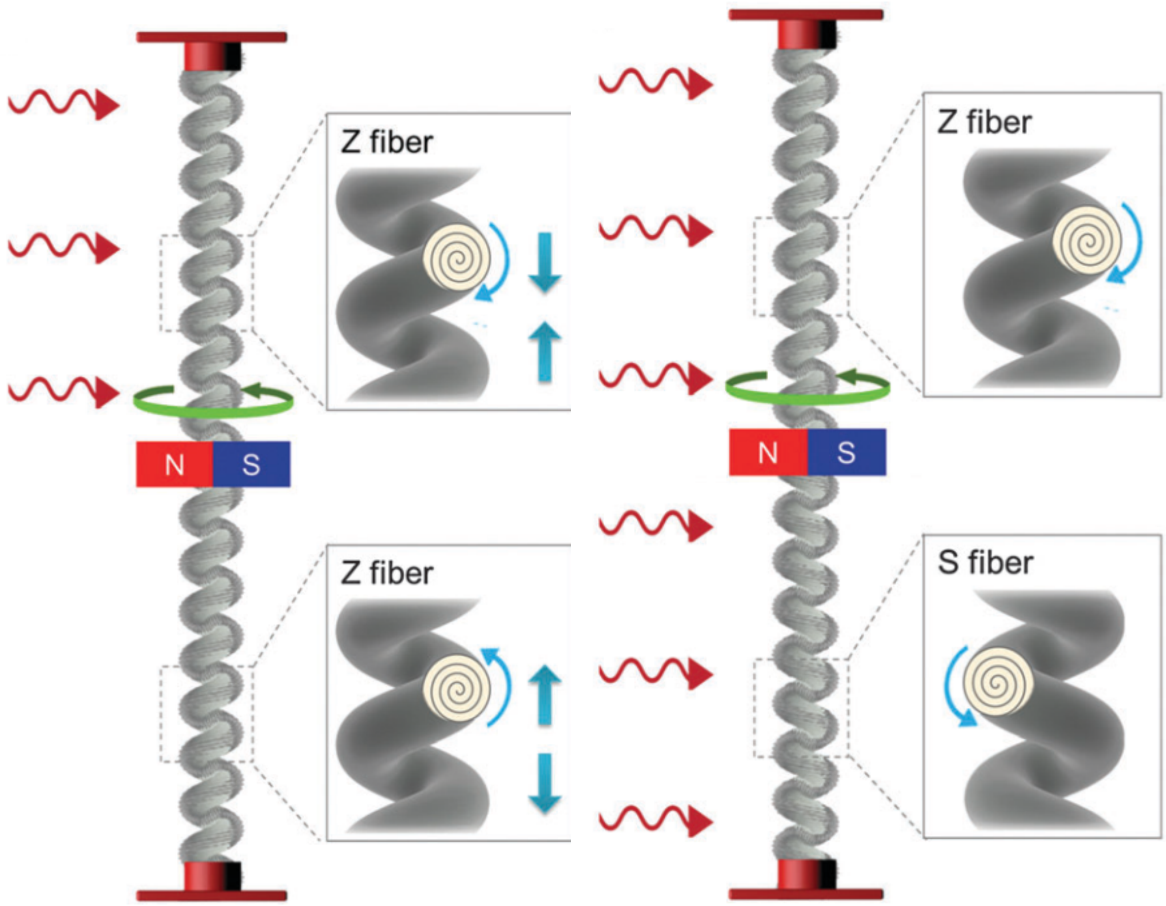

(a) (b)

Figure 4.2: Setup of artificial muscle to convert thermal energy to electrical energy. (a) Configuration of ZZ fiber used for torsional energy harvesting (Kim et al., 2015). (b) Configuration of ZZ fiber used for torsional energy harvesting (Kim et al., 2015).

that magnet is connected to two artificial muscles, the top artificial muscle is twisted in 'S ' direction and the bottom artificial muscle is twisted in 'Z ' direction. When they are heated, they both contracted at the same length at different direction. As a result, magnet

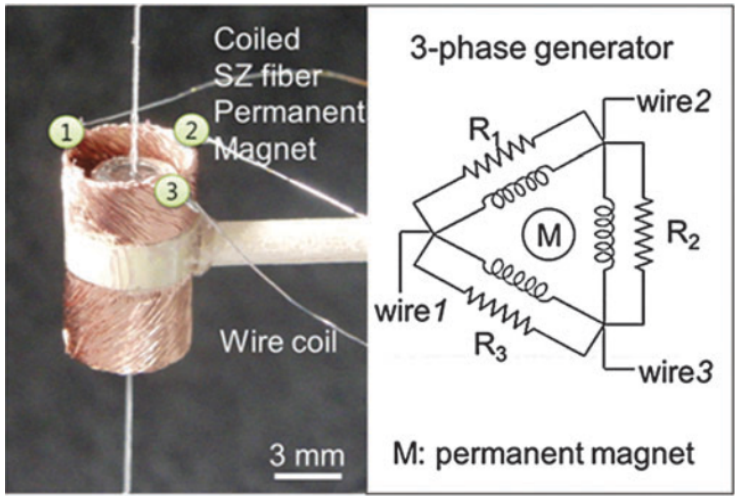

Figure 4.3: Configuration of the 3-phase electricity generator, which use the SZ setup to rotate a co-axial magnet in a set of three coils (left). In order to determine the output power, the resistors were connected to each coil, which is shown in the schematic diagram (right) (Kim et al., 2015).

does not have vertical displacement and it just rotates. Magnet is put in a three-phase, delta-type coil generator so that the movement of magnet affected by the artificial muscle and torque generated by the coil, as shown in Figure 4.3. When the magnet rotates, the coils around the magnet will generate voltage and current, which in turn generates magnetic field to induce force on the magnet to alter the linear and angular accelerations of the magnet. The mechanical schematic graph is shown in Figure 4.4. In this section, we will build mathematical model to study transfer efficiency of such set-up and how paymasters of artificial muscle and magnet affect transfer efficiency.

4.2.1 Dynamics Equation for Magnet

When building this mathematical model, we consider it like this: artificial muscle can be treated as helical spring (Mirvakili et al., 2014; Kim et al., 2015; Yang and Li, 2016), the book (Rao and Yap, 2011) has shown that how does magnet rotate when it is hang by helical spring. When studying the torque and force acting on the magnet, we can see the force generated on magnet is canceled due to the tendency of contraction of artificial muscle when heated.

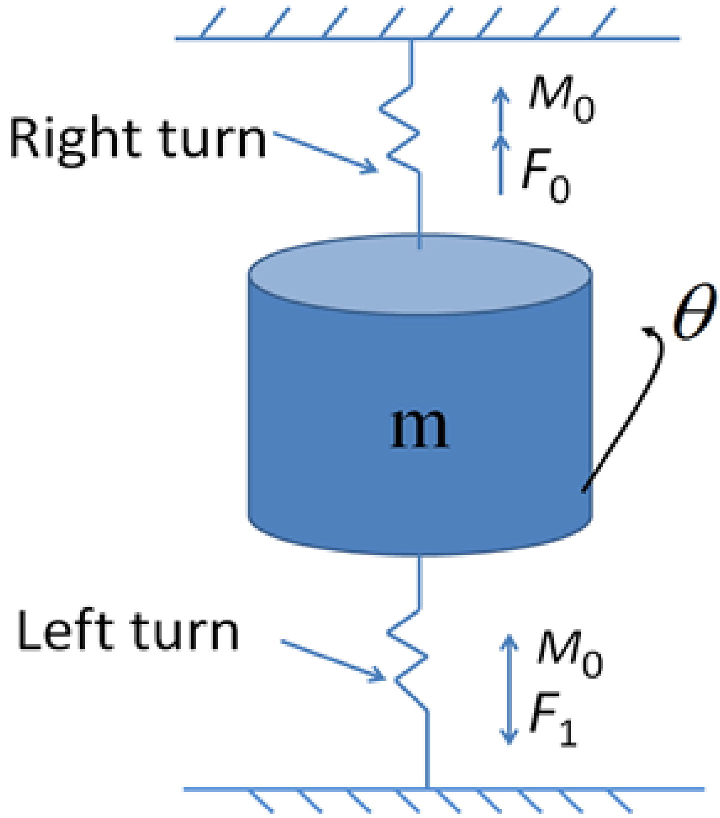

Figure 4.4: Schematic of artificial muscle generator working mechanism

The torque acting on magnet includes inertia torque of magnet, damping torque, torque generated by spring to hinder the rotation of magnet, torque stored in artificial muscle due to inserting coil, which will release when the two segments are heated, and torque generated by coil, which hinders the rotation of magnet. According to the analysis, the equilibrium torque equation of magnet can be expressed as follows:

$$I_0\ddot{\theta}(t) + 2\zeta\sqrt{I_0 K_r}\dot{\theta}(t) + 2K_r\theta(t) = 2M_0(t) - \tau(t) \tag{4.1}$$

Here I_0 is the moment of inertia of the magnet and $I_0 = \frac{1}{2}mr^2$, m is mass of magnet and r is radius of magnet; ζ is damping ratio of wire, K_r, K_e are rotational stiffness and extensional stiffness of the spring, respectively. $M_0(t)$ is torsion torque stored in muscle and release the stored torque due to heat and $F_0(t)$ is the static axial tension, τ(t) is torque due to the coupling between the coil and magnet. At time $t = 0$, no heat is introduced into the system, so the magnet does not have rotation angle and rotation speed. As a result, the following initial condition are given:

$$\begin{aligned} \theta(0) &= 0 \\ \dot{\theta}(0) &= 0 \end{aligned} \tag{4.2}$$

4.2.2 Equations for Nylon Artificial Muscle

We assume that nylon artificial muscle with length L_t is uniformly heated. The force and moment induced by heat are derived. Figure 4.5 shows a model of helical spring due to applied force F_0 and torque M_0. The compressive force F_0 generates two components of the moment acting on a spring wire. At any cross-section the wire is subjected to a tension $F_0 sin(\gamma_0)$, a shearing force $F_0 cos(\gamma_0)$, a twisting moment M_τ and a bending moment M_N , given as

$$\begin{aligned} M_\tau &= M cos\gamma_0 + M_0 sin\gamma_0 \\ M_N &= M sin\gamma_0 - M_0 cos\gamma_0 \end{aligned} \tag{4.3}$$

And $M = F_0 D_0/2$, γ_0 is the initial lead angle of spring; D_0 is the nominal diameter of non loaded spring. The total elastic energy resulting from wire bending and twisting equals

$$U = \frac{1}{2} L_t \left(\frac{M_\tau^2}{\beta_\tau} + \frac{M_N^2}{\beta_N}\right) \tag{4.4}$$

β_N is the corresponding flexural rigidity of the wire and $\beta_N = EI$, β_τ is the torsional rigidity and $\beta_\tau = GJ_0$. Here E, G, I, J_0 are Young's modulus, shear modulus, inertia moment and polar inertia moment, respectively. L_t is total length of wire and $L_t = \pi D_0 n_t / cos\gamma_0$. n_t is the number of heating coils of wire.

According to Castigliano's second theorem, the overall extension δ and twisting angle θ_1 about the spring axis (Wittrick, 1966; Michalczyk, 2009) are given as follows:

$$\begin{aligned} &\delta = \tfrac{\partial U}{\partial F_0}, \theta_1 = \tfrac{\partial U}{\partial M_0} \\ &\delta = f_e F_0 + g_1 M_0 \\ &\theta_1 = f_r M_0 + g_1 F_0 \end{aligned} \tag{4.5}$$

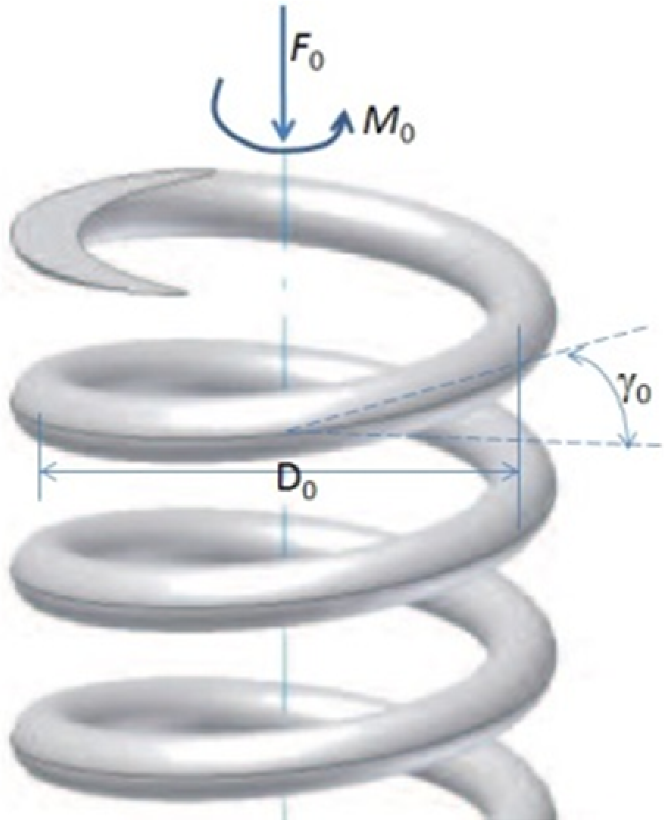

Figure 4.5: A model of ideal helical spring.

Where the "flexibilities" f_e, f_r and g_1 are given by the equations

$$
\begin{aligned}
f_e &= L_t(\tfrac{D_0}{2})^2(\tfrac{cos^2\gamma_0}{\beta_\tau} + \tfrac{sin^2\gamma_0}{\beta_N}) \\
f_r &= L_t(\tfrac{D_0}{2})^2(\tfrac{sin^2\gamma_0}{\beta_\tau} + \tfrac{cos^2\gamma_0}{\beta_N}) \\
g_1 &= L_t\tfrac{D_0}{2}(\tfrac{1}{\beta_\tau} - \tfrac{1}{\beta_{beta_N}})
\end{aligned}
\tag{4.6}
$$

On solving above equations for F_0 and M_0, we have

$$
\begin{aligned}
F_0 &= K_e\delta + C\theta_1 \\
M_0 &= K_r\theta_1 + C\delta
\end{aligned}
\tag{4.7}
$$

Where the stiffness K_e, K_r, C are given by

$$
\begin{aligned}
K_e &= (\beta_\tau cos^2\gamma_0 + \beta_N sin^2\gamma_0)/(L_t R^2) \\
K_r &= (\beta_N cos^2\gamma_0 + \beta_\tau sin^2\gamma_0)/L_t \\
C &= (\beta_\tau - \beta_N)sin\gamma_0 cos\gamma_0/(L_t R)
\end{aligned}
\tag{4.8}
$$

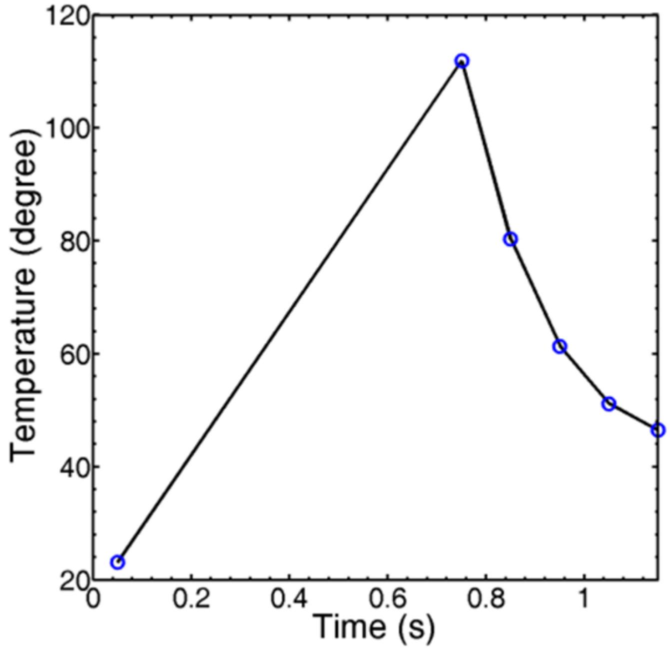

Figure 4.6: Temperature versus time following the application of one hot-air heat pulse.

Where K_e and K_r are the extensional and rotational stiffness of the spring while C is a cross-stiffness and $R = D_0/2$. In our case, heating induced temperature $T(t)$ can be measured, which is shown in Figure 4.6. If the helical spring is in free standing, the elongation and rotation are given as follows:

$$\begin{aligned} &\delta(t) = H_t k_H (T(t) - T_0) sin\gamma_0 \\ &\theta_1 = \tfrac{H_t k_H (T(t) - T_0) cos\gamma_0}{R} \end{aligned} \tag{4.9}$$

In this paper, $H_t = L_t$ is the heated length. This will generate a constraint force $F_0(t)$ and moment $M_0(t)$. k_H is the coefficient of thermal expansion; T_0 is reference temperature. Bring Equation (4.9) to Equation (4.7), F_0 and M_0 can be solved. When M_0 is known, Equation (4.1) can be solved by knowing $\tau(t)$ in the following section.

4.2.3 Voltage Generated in Coil

Due to the movement of magnet, magnetic field near the coil changes, which further induce current and voltage in these three-phase coil. However, the torque generated by the coupling interaction between magnet and coil will hinder the movement of the magnet. Magnet field (Furlani, 2001; Fitzgerald et al., 1992) outside the cylinder magnet is given as follows:

$$B = \mu_0 \frac{M_S}{2} \frac{a^2}{r_1^2} cos(\varphi) \tag{4.10}$$

a is radius of magnet, r_1 is distance between magnet and coil , M_s is magnetization and φ is measured in radians from the magnet pole axis, $\mu_0 = 4\pi^{-7} Hm^{-1}$ is the magnetic constant, N is coil turns. When the magnet field is known, magnet flux can be calculated by the following formula:

$$\Phi = \int_{-\pi/2}^{+\pi/2} Blr_g d\varphi \tag{4.11}$$

Where l is the axial length of the stator and r_g is radius at the air gap.

With the magnet spinning at angular velocity $\omega(t) = \dot{\theta}(t)$, the flux linkage (Fitzgerald et al., 1992) with the stator coil is given as follows:

$$\lambda = N\Phi cos(\theta(t)) \tag{4.12}$$

By Faraday's law, the voltage induced in the stator coil is

$$e_1(t) = \frac{d\lambda}{dt} = -\omega(t)N\Phi sin(\theta(t)) \tag{4.13}$$

Since this is a three-phase generator, the voltages induced in the other two coils can be calculated by using the following formulas:

$$\begin{aligned} e_2(t) &= -\omega(t)N\Phi sin(\theta(t) - \tfrac{2\pi}{3}) \\ e_3(t) &= -\omega(t)N\Phi sin(\theta(t) - \tfrac{4\pi}{3}) \end{aligned} \tag{4.14}$$

4.2.4 Generated Torque due to Electrical Field

The above section has studied that voltages are generated in the three-phase coils due to the movement of magnet. In this section, generated torque is studied due to electrical field .

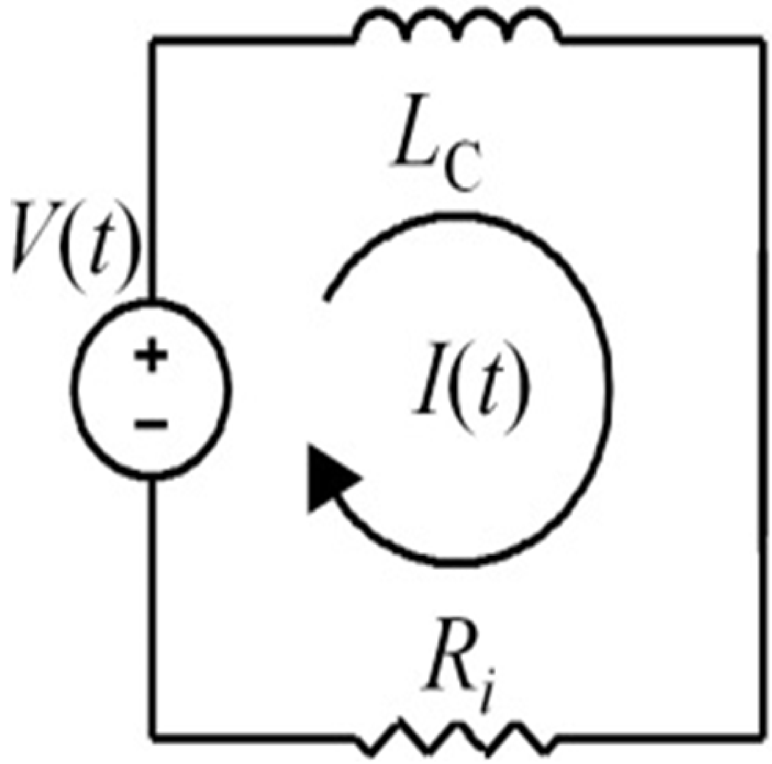

Figure 4.7: Electric circuit of an inductive coil.

Figure 4.7 shows an electric circuit of an inductive coil. The coil features the electrical circuit with inductance L_C and inner resistance R_i. It follows the Kirchhoff's voltage law. The current induced in the stator coil can be calculated by using the following equations (Sneller and Mann, 2010; Cannarella et al., 2011; Ulaby et al., 2014):

$$\begin{aligned} L_{C1}\dot{I}_1(t) + R_{coil}I_1(t) &= e_1(t) \\ L_{C2}\dot{I}_2(t) + R_{coil}I_2(t) &= e_2(t) \\ L_{C3}\dot{I}_3(t) + R_{coil}I_3(t) &= e_3(t) \end{aligned} \tag{4.15}$$

where L_{C1}, L_{C2}, L_{C3} are inductance of the three coils, respectively; R_{coil} is inner resistance, $I_i(t)$ $(i = 1, 2, 3)$ is the electrical current through the circuit and $e_i(t)$ $(i = 1, 2, 3)$ is the induced voltage.

Torque $\tau(t)$ (Furlani, 2001) due to interaction between the coil and magnet can be calculated by following equation:

$$\begin{aligned}\tau(t) = &NI_1(t)\mu_0 M_s l_C \tfrac{a^2}{D_c} cos(\theta(t)) + NI_2(t)\mu_0 M_s l_C \tfrac{a^2}{D_c} cos(\theta(t) - \tfrac{2\pi}{3}) \\ &+NI_3(t)\mu_0 M_s l_C \tfrac{a^2}{D_c} cos(\theta(t) - \tfrac{4\pi}{3})\end{aligned} \tag{4.16}$$

where l_C is the length of each side of the coil, D_c is the radial position of the sides of the coil to the axis of rotation and N is coil turns.

4.2.5 Transfer Efficiency from Kinetic Energy to Electrical Energy

In real life, we expect transfer efficiency from kinetic energy to electrical energy is high. However, the efficiency can be affected by many factors, such as air friction, inner friction of the system and coils and resistance in the generator. In order to make transfer efficiency high, we focus on improving the kinetic energy of magnet by studying parameters of artificial muscle and magnet.

By bringing Equation (4.7) and Equation (4.16) to Equation (4.1), we can calculate the rotation angle. From Equation (4.16), we can see $\tau(t)$ is a complex function expressed by $\theta(t)$ since it concludes terms $I_1(t)cos(\theta(t))$, $I_2(t)cos(\theta(t) - \frac{2\pi}{3})$, $I_3(t)cos(\theta(t) - \frac{4\pi}{3})$. As a result, we cannot get theoretical solution to Equation (4.1), numerical method can be used to solve Equation (4.1) now. During the time period [0,T], the transfer efficiency E can be calculated using the following formula:

$$E(t) = \frac{\sum_{i=1}^{3} \frac{e_i^2(t)}{R}}{\frac{1}{2} I_0 \dot{\theta}^2(t)} \tag{4.17}$$

4.3 Results and Discussion

In this paper, temperature profile $T(t)$ versus time is from experiment shown in Figure 4.6. In the numerical schemes solving process, time step is $\Delta t = 0.00001$ s in the time period [0.05, 1.1]. Eighth degree polynomial interpolation function is used to calculate temperature

Table 4.1: Parameters used in the theoretical calculation of transfer energy efficiency.

E(GPa)	ζ	$k_H(1/°C)$	L_t	$\mu_0(H/m)$	$M_s(A/m)$
3.4	0.1	9×10^{-5}	95	1.26×10^{-6}	4.3×10^5
$r_g(mm)$	$a(mm)$	N	$l(mm)$	$r_1(mm)$	
0.3	1	50	3	$r_g + r$	

at specific time based on experiment temperature profile. Considering the fact that it takes time for heat to travel through the nylon artificial muscle, we shift the temperature profile to the right a little bit. All other parameters used to solve this mechanical-electrical model are listed in Table 4.1.

The predicted voltage versus time profile in Figure 4.8a shows exceptional agreement with experimental voltage versus time profile. The output power is determined by connecting equivalent load resistors to each coil. The experimental oscillating output voltages is produced due to the three-phase alternating current, with a maximum open-circuit, single-phase voltage of 0.160 V, which is very close to numerically solved 0.156 V.

Transfer efficiency is calculated by dividing average electrical energy in the three-phase generator by average kinematic energy in the whole time period, which is different from the method used in (Kim et al., 2015).

$$E = \frac{\sum_{i=1}^{3} \frac{1}{N_1} \sum_{j=0}^{N_1-1} \frac{e_i^2(t_0+j\Delta t)}{R}}{\frac{1}{N_1} \sum_{j=0}^{N_1-1} \frac{1}{2} I_0 \dot{\theta}^2 (t_0 + j\Delta t)} \tag{4.18}$$

Using this formula, the numerical transfer efficiency equals 20.87%, which is lower than the reported transfer efficiency range [43.6%, 97.2%] for the reason that the calculation methods for total kinematic energy are different. In the paper (Kim et al., 2015), n-th peak of torsional angular velocity is selected for calculating kinematic energy when the generator is operated open circuit.

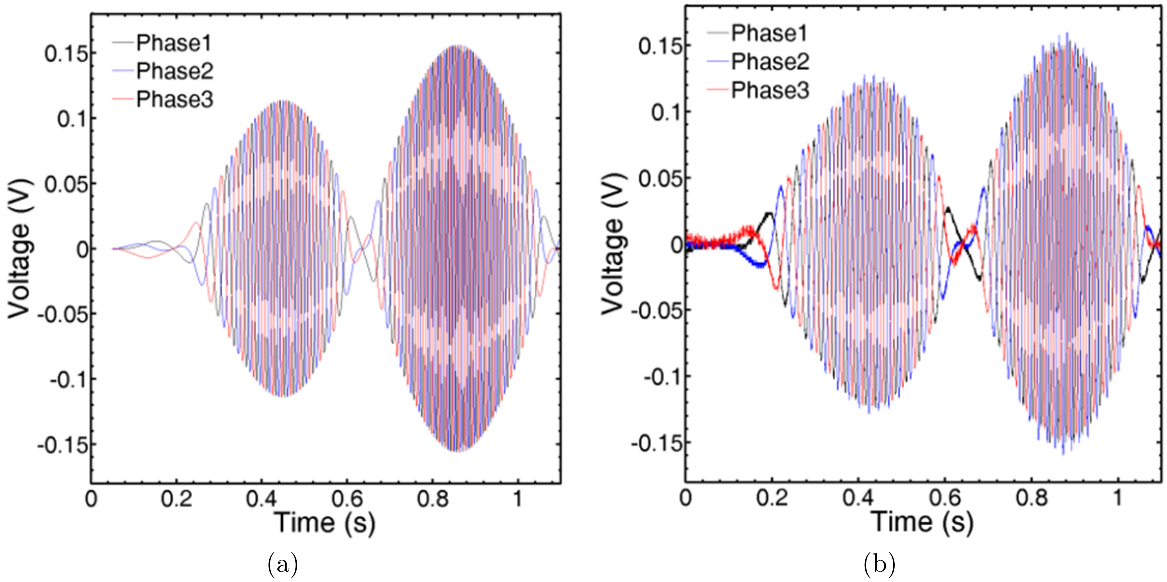

Figure 4.8: Electricity generation from $90°C$ temperature fluctuations using torsional rotation of a magnetic rotor driven by a fully-heated, coiled SZ fiber. (a) Numerical open circuit voltage versus time. (b) The time dependence of experimental open circuit voltage for each of the three coils during heating with a single hot air pulse to $90°C$ above ambient temperature.

In order to increase the transfer efficiency, it is necessary to optimize the design of the experimental device. Artificial muscle (wire) diameter, lead angle of coiled artificial muscle, magnet mass and magnet radius have effects on kinematic energy. Optimal parameters combination can be numerically searched when given the scope of each parameter by using mechanical-electrical model to make the kinetic energy largest. Search range of wire diameter, lead angle, magnet mass, and magnet radius are from 15 μm to 375 μm, 45° to 75°, 0.5 g to 12.5 g, and 0.5 mm to 12.5 mm, respectively. The numerical result shows that when $D_0 = 375\ \mu m$, $\gamma_0 = 48°$, $m = 6\ g$ and $r = 7\ mm$ produce the largest kinetic energy large 22.47 J. When searching the best parameters combination, we set step interval for each parameter large in order to save computation time. After finding the optimum parameters combination by using big step interval, another round of search with small interval is conducted to find specific number. The narrowed down search scopes for wire diameter, lead

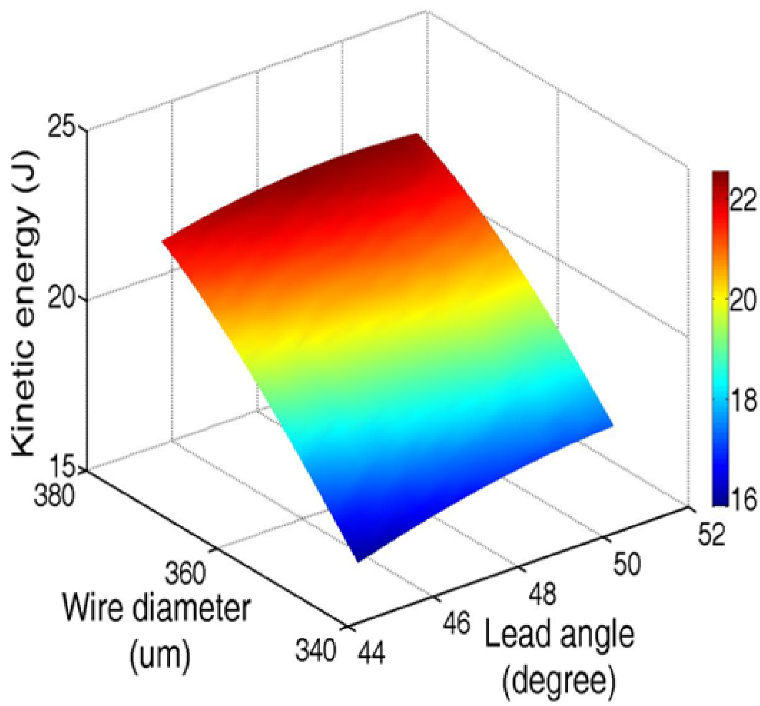

Figure 4.9: Kinetic energy versus wire diameter and lead angle of a magnet rotor driven by fully-heated, coiled SZ fiber.

angle, magnet mass, and magnet radius are: $D_0 : 345 - 375\ \mu m$; $\gamma_0 : 45° - 51°$; $m : 5.5 - 6.5\ g$; $r : 6.5 - 7.5\ mm$, respectively. The kinematic energy versus different parameters are shown in Figure 4.9 - Figure 4.14.

When study how kinetic energy changes with wire diameter and lead angle, magnet mass and radius are fixed: $m = 6\ g$, $r = 7\ mm$. Figure 4.9 shows that kinetic energy almost linearly increase with wire diameter, which is consistent with experiment observation (Kim et al., 2015). This result can be interpreted in such way: heating rate reciprocally relies on wire diameter, while heat flux is proportional to surface area, as a result a temperature change generated by heat quadratically depends on wire diameter. However, lead angle does not have obvious effect on the kinematic energy during the search range.

Figure 4.10 shows kinetic energy changes with wire diameter and magnet mass under the condition that $r = 7\ mm$ and $\gamma_0 = 48°$, kinetic energy increases as wire diameter increase no matter the magnet mass. Kinematic energy depends on the moment inertia of magnet and

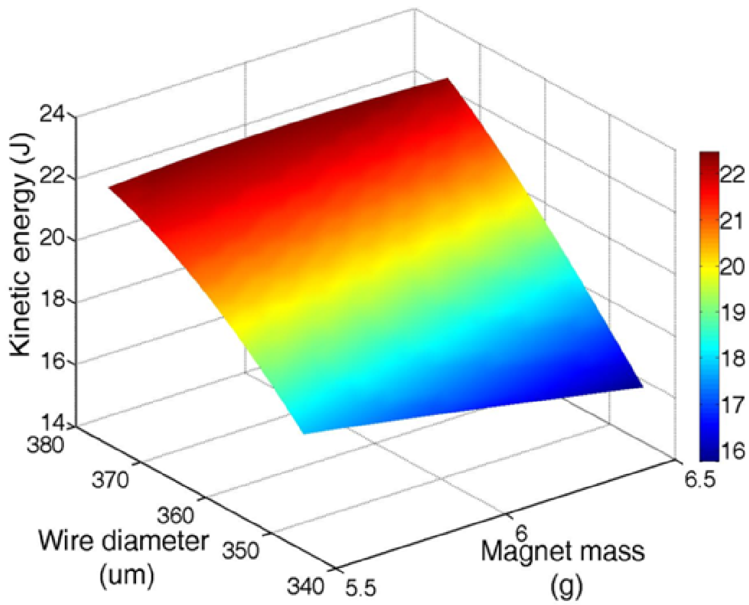

Figure 4.10: Kinetic energy versus wire diameter and magnet mass of a magnet rotor driven by fully-heated, coiled SZ fiber.

torsional speed. Moment of inertia of magnet is proportional to the magnet mass, however it does not mean large magnet mass can result in the biggest kinetic energy for the reason that magnet mass reversely affect torsional speed. Hence there exists an optimum magnet mass to optimize the kinetic energy.

Figure 4.11 shows that kinetic energy changes with wire diameter and magnet radius mass under the condition that $m = 6\ g$, $\gamma_0 = 48°$. It describes that kinetic energy increases with wire diameter at any magnet radius. Moment of inertia of magnet quadratically depends on magnet radius, and kinetic energy linearly depends on moment of inertia. However, when the magnet radius is too big, it will result in big air friction so that damping ratio of such system will be high. As a result, the rotation speed of the magnet will decrease. Hence there exists an optimum magnet radius to optimize the kinetic energy.

Figure 4.12 shows that kinetic energy changes with lead angle and magnet mass under the condition that $r = 7\ mm$ and $D_0 = 375\ \mu m$. It shows that kinetic energy increases

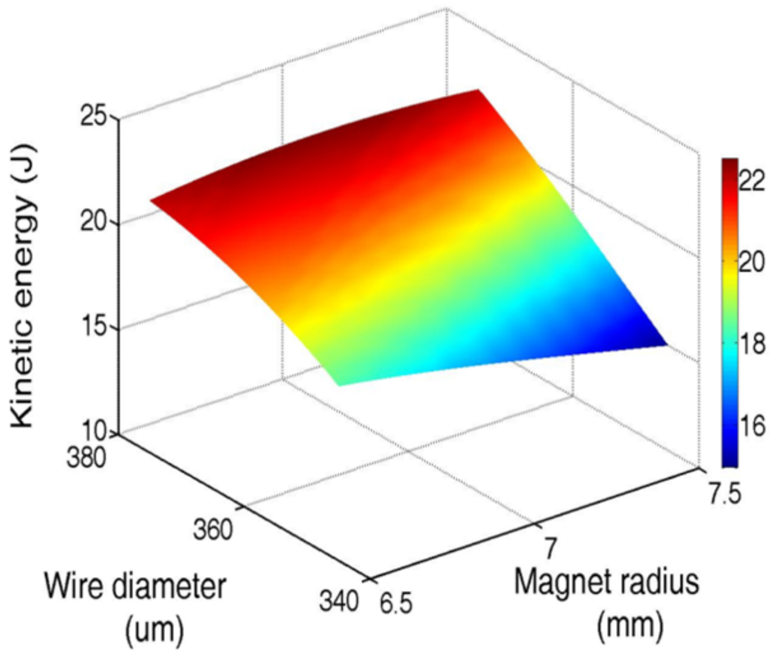

Figure 4.11: Kinetic energy versus wire diameter and magnet radius of a magnet rotor driven by fully-heated, coiled SZ fiber.

first and then decreases as lead angle and magnet mass increase. Kinetic energy achieves its maximal value at middle point.

Figure 4.13 shows that kinetic energy changes with lead angle and magnet radius under the condition that $m = 6\ g$, $D_0 = 375\ \mu m$. It shows that kinetic energy increases first and then decreases as lead angle and magnet radius increase. Kinetic energy achieves its maximal value at middle point.

Figure 4.14 shows that kinetic energy changes with magnet mass and magnet radius under the condition that $D_0 = 375\ \mu m$ and $\gamma_0 = 48°$. It shows that kinetic energy achieves its maximal value at middle point. Figure 4.13 and Figure 4.14 show us that optimal parameter combination of four variables can generate large voltage.

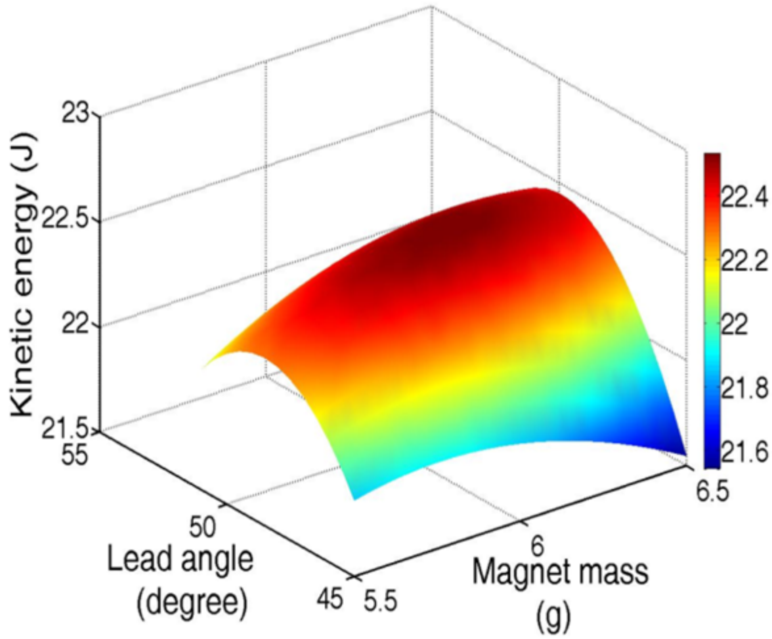

Figure 4.12: Kinetic energy versus lead angle and magnet mass of a magnet rotor driven by fully-heated, coiled SZ fiber.

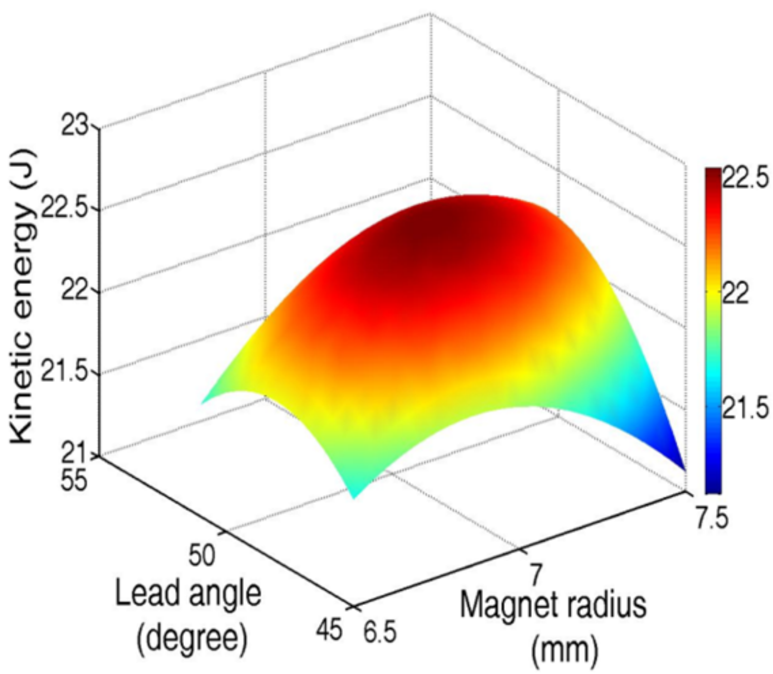

Figure 4.13: Kinetic energy versus lead angle and magnet radius of a magnet rotor driven by fully-heated, coiled SZ fiber.

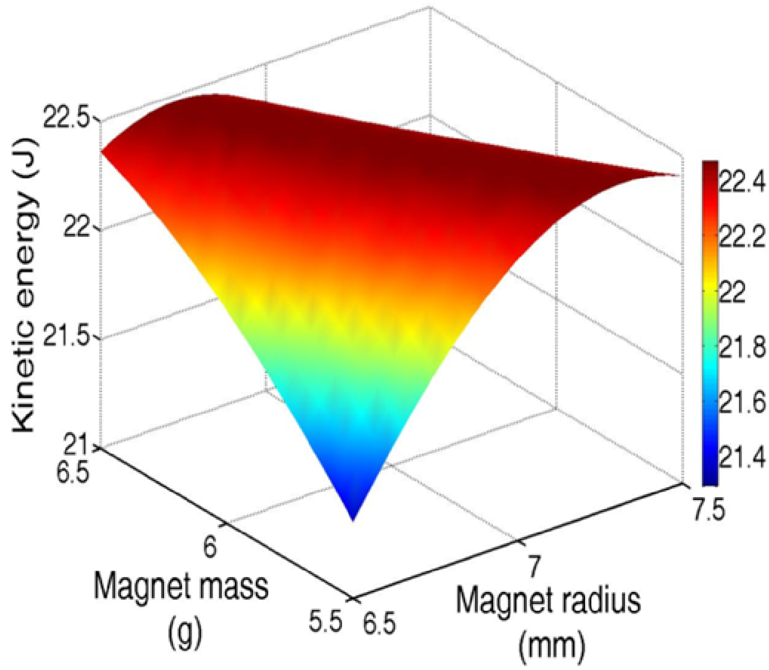

Figure 4.14: Kinetic energy versus magnet mass and magnet radius of a magnet rotor driven by fully-heated, coiled SZ fiber.

4.4 Conclusions

In this chapter, coiled nylon artificial muscle is connected to a rotor in three-phase, delta-type coil generator, which can transfer kinematic energy to electrical energy. In order to investigate transfer efficiency of such newly designed set-up, mechanical electrical model is built. All the torque acted on magnet is studied, including inertia torque of magnet, damping torque, torque generated by spring to hinder the rotation of magnet, torque stored in artificial muscle due to inserting coil, which will release when the two segments are heated, and torque generated by coil, which hinders the rotation of magnet. Torque balance equation is a variable dependent implicit equation, theoretical solution is difficult to find and numerical method can be used to solve such equation. Experimental three-phase voltage versus time and numerical three-phase voltage time profile are extremely matched each other. Transfer efficiency reported in this section is lower than that in published paper (Kim et al., 2015) for the reason that the method used to calculate kinetic energy is different. In order to optimize kinetic energy of the magnet, effects of parameters of artificial muscle and magnet are studied. Numerical result shows that kinetic energy is linearly dependent on diameter of coiled artificial muscle, which is consistent with experiment observation. Larger diameter of coiled artificial muscle means larger spring index, which is good for energy transfer. There exist the optimum magnet mass and radius for the reason that even though magnet mass and radius positively affect kinetic energy, they both negatively affect torsional speed. Lead angle in this range does not show obvious effect on kinetic energy. All parameters affect the kinetic energy independently, the effect will not change with parameter combination.

CHAPTER 5

CONCLUSIONS AND PERSPECTIVE

5.1 Conclusions

Fiber reinforced composite usually has very high tensile strength, however, the compressive strength is only half of its tensile strength. Since during compression, matrix failure, interface debonding or fiber microbuckling usually happens. In order to improve the interfacial shear strength during compression, a newly robust method is developed by wrapping CNT sheet around carbon fiber and then embedding into epoxy. From current experiment results, they show that interfacial shear strength increased by 40% to 100% compared to baseline date. In order to investigate how the interphase region (CNT nanocomposite) affect the compressive strength, composite microbuckling model is built. A new type of twisted and coiled CNT yarns artificial muscle is designed by coating polymer on the CNT yarns, which can provide much higher performance due to fully use of the muscle. Mathematical model is built to investigate the reason why performance of polymer coated CNT yarns is very excellent. The work capacity of these two types of artificial muscles (polymer coated CNT yarn artificial muscle and polymer infiltrated CNT yarn artificial muscle) is also studied. Low-cost, high-performance energy harvester made of fishing line and sewing thread can be used to harvest electrical energy from low-temperature waste energy sources. In order to make fishing line and sewing thread to do actuation, amount of twist is inserted in to the muscle and high temperature oven is used to make the muscle keep shape. SZ artificial muscle can harvest much more energy than ZZ artificial muscle. In order to understand the working mechanism of this type of energy harvester and optimize the design of SZ artificial muscle to make the transfer efficiency much higher, coupled mechanical and electrical model is built.

In Chapter 2, the composite under compression in the buckling analysis model is consist of three parts: carbon fiber, CNT nanocomposite (interphase region) and epoxy. Two different constitutive model is used, one is transversely isotropic model for carbon fiber and the other is isotropic model for CNT nanocomposite and matrix. Plain strain condition is applied to analysis and small perturbation in the field equation is used in buckling analysis. Boundary conditions of force and traction are given based on the assumption that perfect bonding interface exists between fiber and interphase region, and between interphase region and matrix. The result shows that buckling strain of modeling fiber as anisotropic is 58% much lower than buckling strain of modeling fiber as isotropic. As long as the interphase region's modulus is much higher than matrix's Young's modulus, adding CNT sheet between fiber and matrix can increase the compressive strength. And the optimum interphase region thickness equals fiber diameter when fiber volume fraction dominates such composite.

In Chapter 3, two equilibrium states are studies, one is non-actuated state and the other one is actuated state. In both two states, torque on the CNT core is balanced by the opposing torque in the elastically twisted polymer. Two mechanistic contributions to the torsional actuation of polymer coated twisted CNT yarn are captured in the theory: polymer swelling and softening combined to partially release elastically stored torsional energy in the core yarn. The theory also shows that the capability of the polymer to compress core and keeping the twist of the core limited by polymer thickness to core diameter ratio. However, very high polymer thickness to core diameter ratio will constrain the release of such inserted twisted after polymer coated CNT yarn is actuated. As a result, an optimum polymer thickness to core diameter ratio exists to maximize torsional stroke. Theoretically predicted maximum torsional stroke is 151°/mm for a polymer thickness to core diameter ratio of 0.15. The predicted ratio of the maximum contractile work capacity of the polymer coated core to that of the polymer infiltrated core is 1.52.

In Chapter 4, this new type of coiled artificial muscle is treated as helical spring. When heat pulse is uniformly distributed to two segments of coiled artificial muscle, how the stored torque in artificial muscle releases based on given temperature profile is studied. Torques exerted on magnet include inertia torque of magnet, damping torque, torque generated by spring to hinder the rotation of magnet, stored torque releasing due to heat, and torque due to electrical field, torque balance equation is build. In order to solve this second order differential equation, torque generated by electrical filed must be investigated, hence, the electrical field equation for three phase coils is studied. Transfer efficiency for such system is given, and in order to improve transfer efficiency, we use optimization method to find the best combination of parameters. It shows that the transfer efficiency increases with artificial muscle diameter, which is very consistent with experiment observation. Lead angle of coiled muscle do not have obvious effect on transfer efficiency based on the scope we choose. There exist optimum magnet mass and magnet radius to maximize kinetic energy.

5.2 Perspective

5.2.1 Model for Composite under Compression

In the model for buckling analysis, the only carbon fiber is considered as transversely isotropic, however, the interphase region (nanocomposite) can also be anisotropic, and the anisotropic material parameters can be calculated by nanoindentation and finite element simulation. And current model is validate for small volume fraction of carbon fiber. Carbon fiber composites widely used in industry usually have volume fraction more than 60 %, hence a new model considering large carbon fiber volume fraction and interphase region is needed. And carbon fibers also experience misalignment under compression, as a result composite kinking model considering this new structure containing interphase region is also an interesting research direction.

5.2.2 Polymer Coated CNT Yarn

In this dissertation, two different actuators: one is polymer coated CNT yarn and the other one is polymer infiltrated CNT yarn, are investigated. For vapor-driven torsional actuation, an optimum polymer thickness to fiber diameter ratio is predicted by theory. Modulus decreasing and diameter of polymer coated core increasing with vapor absorption are considered in the model. For vapor-driven tensile actuation, optimum load exists initial contractile stroke (ΔL_0) and elongation of muscle due to loss of stiffness competing with each other. If the polymer is partially infiltrated in to the CNT yarn, whether this topology will show higher performance than that of polymer coated and polymer fully infiltrated CNT yarn. And what's the best partially infiltrated polymer's volume fraction for the best performance of actuation. All these are remained but very interesting problems, which can be investigated in future.

5.2.3 Nylon Artificial muscle

In this dissertation, we already consider the whole energy harvesting process. Transfer efficiency from mechanical energy to electrical energy already calculated and remarkable agreement between experimentally measured and theoretically calculated voltage are already shown in Chapter 4. Optimal method is used to study the parameters effect in order to improve the design of energy harvester in macroscale. In fact, polymer chain bias angle on the twisted, non-coiled muscles surface with respect to the fiber direction has effect on the torsional stroke and transfer efficiency. A model coupling the mesoscale and macroscale can predict how the bias angle affect the performance artificial muscle.

REFERENCES

Agrawal, S., K. K. Singh, and P. Sarkar (2014). Impact damage on fibre-reinforced polymer matrix composite–a review. *Journal of Composite Materials 48*(3), 317–332.

Aliev, A. E., J. Oh, M. E. Kozlov, A. A. Kuznetsov, S. Fang, A. F. Fonseca, R. Ovalle, M. D. Lima, M. H. Haque, Y. N. Gartstein, et al. (2009). Giant-stroke, superelastic carbon nanotube aerogel muscles. *science 323*(5921), 1575–1578.

Amirtharajah, R. and A. P. Chandrakasan (1998). Self-powered signal processing using vibration-based power generation. *IEEE journal of solid-state circuits 33*(5), 687–695.

Andrianov, I. V., A. L. Kalamkarov, and D. Weichert (2012). Buckling of fibers in fiber-reinforced composites. *Composites Part B: Engineering 43*(4), 2058–2062.

Assael, M. J., K. D. Antoniadis, I. N. Metaxa, and D. Tzetzis (2008). Measurements on the enhancement of the thermal conductivity of an epoxy resin when reinforced with glass fiber and carbon multiwalled nanotubes. *Journal of Chemical & Engineering Data 54*(9), 2365–2370.

Bai, Z., Y. Su, and B. Ji (2016). Buckling behaviors of staggered nanostructure of biological materials. *Journal of Applied Mechanics 83*(3), 031011.

Barber, A. H., S. R. Cohen, A. Eitan, L. S. Schadler, and H. D. Wagner (2006). Fracture transitions at a carbon-nanotube/polymer interface. *Advanced Materials 18*(1), 83–87.

Barber, A. H., S. R. Cohen, and H. D. Wagner (2003). Measurement of carbon nanotube–polymer interfacial strength. *Applied Physics Letters 82*(23), 4140–4142.

Bates, J., G. Gruzalski, and C. Luck (1993). Rechargeable solid state lithium microbatteries. In *Micro Electro Mechanical Systems, 1993, MEMS'93, Proceedings An Investigation of Micro Structures, Sensors, Actuators, Machines and Systems. IEEE.*, pp. 82–86. IEEE.

Baughman, R. H., C. Cui, A. A. Zakhidov, Z. Iqbal, J. N. Barisci, G. M. Spinks, G. G. Wallace, A. Mazzoldi, D. De Rossi, A. G. Rinzler, et al. (1999). Carbon nanotube actuators. *Science 284*(5418), 1340–1344.

Beeby, S. P., R. Torah, M. Tudor, P. Glynne-Jones, T. O'donnell, C. Saha, and S. Roy (2007). A micro electromagnetic generator for vibration energy harvesting. *Journal of Micromechanics and microengineering 17*(7), 1257.

Beeby, S. P., M. J. Tudor, and N. White (2006). Energy harvesting vibration sources for microsystems applications. *Measurement science and technology 17*(12), R175.

Bekyarova, E., E. Thostenson, A. Yu, H. Kim, J. Gao, J. Tang, H. Hahn, T.-W. Chou, M. Itkis, and R. Haddon (2007). Multiscale carbon nanotube- carbon fiber reinforcement for advanced epoxy composites. *Langmuir 23*(7), 3970–3974.

Bekyarova, E., E. T. Thostenson, A. Yu, M. E. Itkis, D. Fakhrutdinov, T.-W. Chou, and R. C. Haddon (2007). Functionalized single-walled carbon nanotubes for carbon fiber-epoxy composites. *The Journal of Physical Chemistry C 111*(48), 17865–17871.

Budiansky, B. and N. A. Fleck (1993). Compressive failure of fibre composites. *Journal of the Mechanics and Physics of Solids 41*(1), 183–211.

Cannarella, J., J. Selvaggi, S. Salon, J. Tichy, and D.-A. Borca-Tasciuc (2011). Coupling factor between the magnetic and mechanical energy domains in electromagnetic power harvesting applications. *IEEE Transactions on Magnetics 47*(8), 2076–2080.

Cao, X., W.-J. Chiang, Y.-C. King, and Y.-K. Lee (2007). Electromagnetic energy harvesting circuit with feedforward and feedback dc–dc pwm boost converter for vibration power generator system. *IEEE Transactions on Power Electronics 22*(2), 679–685.

Che, J., W. Yuan, G. Jiang, J. Dai, S. Y. Lim, and M. B. Chan-Park (2009). Epoxy composite fibers reinforced with aligned single-walled carbon nanotubes functionalized with generation 0- 2 dendritic poly (amidoamine). *Chemistry of materials 21*(8), 1471–1479.

Cheng, Q., B. Wang, C. Zhang, and Z. Liang (2010). Functionalized carbon-nanotube sheet/bismaleimide nanocomposites: Mechanical and electrical performance beyond carbon-fiber composites. *Small 6*(6), 763–767.

Ching, N. N., G. M. Chan, W. J. Li, H. Y. Wong, and P. H. Leong (2000). Pcb integrated micro-generator for wireless systems. In *Intl. Symp. on Smart Structures and Microsystems*, pp. 19–21.

Cook-Chennault, K., N. Thambi, and A. Sastry (2008). Powering mems portable devicesa review of non-regenerative and regenerative power supply systems with special emphasis on piezoelectric energy harvesting systems. *Smart Materials and Structures 17*(4), 043001.

Courty, S., J. Mine, A. Tajbakhsh, and E. Terentjev (2003). Nematic elastomers with aligned carbon nanotubes: New electromechanical actuators. *EPL (Europhysics Letters) 64*(5), 654.

Deng, J., J. Li, P. Chen, X. Fang, X. Sun, Y. Jiang, W. Weng, B. Wang, and H. Peng (2015). Tunable photothermal actuators based on a pre-programmed aligned nanostructure. *Journal of the American Chemical Society 138*(1), 225–230.

Ding, W., A. Eitan, F. Fisher, X. Chen, D. Dikin, R. Andrews, L. Brinson, L. Schadler, and R. Ruoff (2003). Direct observation of polymer sheathing in carbon nanotube- polycarbonate composites. *Nano letters 3*(11), 1593–1597.

Drzal, L. (1990). The role of the fiber-matrix interphase on composite properties. *Vacuum 41*(7-9), 1615–1618.

Duan, Q., S. Sorooshian, and V. K. Gupta (1994). Optimal use of the sce-ua global optimization method for calibrating watershed models. *Journal of hydrology 158*(3-4), 265–284.

Eftekhari, M. and A. Fatemi (2015). Tensile, creep and fatigue behaviours of short fibre reinforced polymer composites at elevated temperatures: a literature survey. *Fatigue & Fracture of Engineering Materials & Structures 38*(12), 1395–1418.

Faes, J. C., A. Rezaei, W. Van Paepegem, and J. Degrieck (2015). Influence of matrix toughness and interfacial strength on the toughness of epoxy composites with ductile steel fabric reinforcement. *Composite Interfaces 22*(8), 779–793.

Fan, Z., M. H. Santare, and S. G. Advani (2008). Interlaminar shear strength of glass fiber reinforced epoxy composites enhanced with multi-walled carbon nanotubes. *Composites Part A: Applied Science and Manufacturing 39*(3), 540–554.

Fang, H.-B., J.-Q. Liu, Z.-Y. Xu, L. Dong, L. Wang, D. Chen, B.-C. Cai, and Y. Liu (2006). Fabrication and performance of mems-based piezoelectric power generator for vibration energy harvesting. *Microelectronics Journal 37*(11), 1280–1284.

Fitzgerald, A. E., C. Kingsley, S. D. Umans, J. Yescas Milanés, R. Navarro Salas, et al. (1992). *Electric machinery. Máquinas eléctricas*.

Furlani, E. P. (2001). *Permanent magnet and electromechanical devices: materials, analysis, and applications*. Academic press.

Ganesan, Y., C. Peng, Y. Lu, P. E. Loya, P. Moloney, E. Barrera, B. I. Yakobson, J. M. Tour, R. Ballarini, and J. Lou (2011). Interface toughness of carbon nanotube reinforced epoxy composites. *ACS applied materials & interfaces 3*(2), 129–134.

Godara, A., L. Gorbatikh, G. Kalinka, A. Warrier, O. Rochez, L. Mezzo, F. Luizi, A. Van Vuure, S. Lomov, and I. Verpoest (2010). Interfacial shear strength of a glass fiber/epoxy bonding in composites modified with carbon nanotubes. *Composites Science and Technology 70*(9), 1346–1352.

Godara, A., L. Mezzo, F. Luizi, A. Warrier, S. V. Lomov, A. Van Vuure, L. Gorbatikh, P. Moldenaers, and I. Verpoest (2009). Influence of carbon nanotube reinforcement on the processing and the mechanical behaviour of carbon fiber/epoxy composites. *Carbon 47*(12), 2914–2923.

Greszczuk, L. (1975). Microbuckling failure of circular fiber-reinforced composites. *AIAA Journal 13*(10), 1311–1318.

Hahn, H. and M. Sohi (1986). Buckling of a fiber bundle embedded in epoxy. *Composites science and technology 27*(1), 25–41.

Haines, C. S., M. D. Lima, N. Li, G. M. Spinks, J. Foroughi, J. D. Madden, S. H. Kim, S. Fang, M. J. de Andrade, F. Göktepe, et al. (2014). Artificial muscles from fishing line and sewing thread. *science 343*(6173), 868–872.

Harich, J., Y. Lapusta, and W. Wagner (2009). 3d fe-modeling of surface and anisotropy effects during micro-buckling in fiber composites. *Composite structures 89*(4), 551–555.

He, H., J. Wang, K. Li, J. Wang, and J. Gu (2010). Mixed resin and carbon fibres surface treatment for preparation of carbon fibres composites with good interfacial bonding strength. *Materials & Design 31*(10), 4631–4637.

Hohlfeld, D., R. Vullers, and J. de Boeck (2008). An electromagnetic energy harvester for low frequency excitation. In *Integration Issues of Miniaturized Systems-MOMS, MOEMS, ICS and Electronic Components (SSI), 2008 2nd European Conference & Exhibition on*, pp. 1–8. VDE.

Huang, Y. and R. J. Young (1996). Interfacial micromechanics in thermoplastic and thermosetting matrix carbon fibre composites. *Composites Part A: Applied Science and Manufacturing 27*(10), 973–980.

Ji, W. and A. M. Waas (2007). Global and local buckling of a sandwich beam. *Journal of engineering mechanics 133*(2), 230–237.

Khaligh, A., P. Zeng, and C. Zheng (2010). Kinetic energy harvesting using piezoelectric and electromagnetic technologiesstate of the art. *IEEE Transactions on Industrial Electronics 57*(3), 850–860.

Kim, O., T. J. Shin, and M. J. Park (2013). Fast low-voltage electroactive actuators using nanostructured polymer electrolytes. *Nature communications 4*, 2208.

Kim, S. H., M. D. Lima, M. E. Kozlov, C. S. Haines, G. M. Spinks, S. Aziz, C. Choi, H. J. Sim, X. Wang, H. Lu, et al. (2015). Harvesting temperature fluctuations as electrical energy using torsional and tensile polymer muscles. *Energy & Environmental Science 8*(11), 3336–3344.

Koeneman, P. B., I. J. Busch-Vishniac, and K. L. Wood (1997). Feasibility of micro power supplies for mems. *Journal of Microelectromechanical systems 6*(4), 355–362.

Kotaki, M., K. Wang, M. L. Toh, L. Chen, S. Y. Wong, and C. He (2006). Electrically conductive epoxy/clay/vapor grown carbon fiber hybrids. *Macromolecules 39*(3), 908–911.

Kyriakides, S., R. Arseculeratne, E. Perry, and K. Liechti (1995). On the compressive failure of fiber reinforced composites. *International Journal of Solids and Structures 32*(6-7), 689–738.

Landi, B., R. Raffaelle, M. Heben, J. Alleman, W. VanDerveer, and T. Gennett (2005). Development and characterization of single wall carbon nanotube–nafion composite actuators. *Materials Science and Engineering: B 116*(3), 359–362.

Lane, R., S. Hayes, and F. Jones (2001). Fibre/matrix stress transfer through a discrete interphase: 2. high volume fraction systems. *Composites science and technology 61*(4), 565–578.

Lapusta, Y., J. Harich, and W. Wagner (2008). Three-dimensional fe model for fiber interaction effects during microbuckling in composites with isotropic and anisotropic fibers. *International Journal for Numerical Methods in Biomedical Engineering 24*(12), 2206–2215.

Lapusta, Y., F. Labesse-Jied, A. Samborskaya, and W. Wagner (2011). On the effects of interacting anisotropic fibers on the microbuckling in a composite. *International Journal of Fracture 167*(1), 103–110.

Lee, D. Y., I.-S. Park, M.-H. Lee, K. J. Kim, and S. Heo (2007). Ionic polymer–metal composite bending actuator loaded with multi-walled carbon nanotubes. *Sensors and Actuators A: Physical 133*(1), 117–127.

Lee, J. B., Z. Chen, M. G. Allen, A. Rohatgi, and R. Arya (1995). A miniaturized high-voltage solar cell array as an electrostatic mems power supply. *Journal of Microelectromechanical Systems 4*(3), 102–108.

Lendlein, A., H. Jiang, O. Jünger, and R. Langer (2005). Light-induced shape-memory polymers. *Nature 434*(7035), 879.

Levitsky, I., P. Kanelos, and W. B. Euler (2004). Electromechanical actuation of composite material from carbon nanotubes and ionomeric polymer. *The Journal of chemical physics 121*(2), 1058–1065.

Li, J. (2008). Interfacial studies on the o3 modified carbon fiber-reinforced polyamide 6 composites. *Applied Surface Science 255*(5), 2822–2824.

Lima, M. D., N. Li, M. J. De Andrade, S. Fang, J. Oh, G. M. Spinks, M. E. Kozlov, C. S. Haines, D. Suh, J. Foroughi, et al. (2012). Electrically, chemically, and photonically powered torsional and tensile actuation of hybrid carbon nanotube yarn muscles. *Science 338*(6109), 928–932.

Liu, Y., K. L. Ren, H. F. Hofmann, and Q. Zhang (2005). Investigation of electrostrictive polymers for energy harvesting. *ieee transactions on ultrasonics, ferroelectrics, and frequency control 52*(12), 2411–2417.

Liu, Z., S. Fang, F. Moura, J. Ding, N. Jiang, J. Di, M. Zhang, X. Lepró, D. Galvão, C. Haines, et al. (2015). Hierarchically buckled sheath-core fibers for superelastic electronics, sensors, and muscles. *Science 349*(6246), 400–404.

Lo, K. and E.-M. Chim (1992). Compressive strength of unidirectional composites. *Journal of Reinforced Plastics and Composites 11*(8), 838–896.

Lu, H., R. H. Baughman, M. H. Haque, and S. D. Fang (2017, September 12). Method of fabricating carbon nanotube sheet scrolled fiber reinforced polymer composites and compositions and uses thereof. US Patent 9,758,628.

Luo, H., S. Roy, and H. Lu (2012). Dynamic compressive behavior of unidirectional im7/5250-4 laminate after thermal oxidation. *Composites Science and Technology 72*(2), 159–166.

Ma, W., L. Liu, Z. Zhang, R. Yang, G. Liu, T. Zhang, X. An, X. Yi, Y. Ren, Z. Niu, et al. (2009). High-strength composite fibers: realizing true potential of carbon nanotubes in polymer matrix through continuous reticulate architecture and molecular level couplings. *Nano letters 9*(8), 2855–2861.

Maligno, A., N. Warrior, and A. Long (2010). Effects of interphase material properties in unidirectional fibre reinforced composites. *Composites Science and Technology 70*(1), 36–44.

Martinez-Rubi, Y., B. Ashrafi, J. Guan, C. Kingston, A. Johnston, B. Simard, V. Mirjalili, P. Hubert, L. Deng, and R. J. Young (2011). Toughening of epoxy matrices with reduced single-walled carbon nanotubes. *ACS applied materials & interfaces 3*(7), 2309–2317.

Matsuki, H., M. Yamaguchi, T. Watanabe, K. Murakami, K. Nadehara, and T. Yamamoto (1988). Implantable transformer for an artificial heart utilizing amorphous magnetic fibers. *Journal of Applied Physics 64*(10), 5859–5861.

Maurin, R., P. Davies, N. Baral, and C. Baley (2008). Transverse properties of carbon fibres by nano-indentation and micro-mechanics. *Applied Composite Materials 15*(2), 61.

Mei, L., X. He, Y. Li, R. Wang, C. Wang, and Q. Peng (2010). Grafting carbon nanotubes onto carbon fiber by use of dendrimers. *Materials letters 64*(22), 2505–2508.

Michalczyk, K. (2009). Analysis of helical compression spring support influence on its deformation. *Archive of Mechanical Engineering 56*(4), 349–362.

Mirfakhrai, T., J. Oh, M. Kozlov, E. C. W. Fok, M. Zhang, S. Fang, R. H. Baughman, and J. D. Madden (2007). Electrochemical actuation of carbon nanotube yarns. *Smart Materials and Structures 16*(2), S243.

Mirvakili, S. M., A. R. Ravandi, I. W. Hunter, C. S. Haines, N. Li, J. Foroughi, S. Naficy, G. M. Spinks, R. H. Baughman, and J. D. Madden (2014). Simple and strong: Twisted silver painted nylon artificial muscle actuated by joule heating. In *Electroactive Polymer Actuators and Devices (EAPAD) 2014*, Volume 9056, pp. 90560I. International Society for Optics and Photonics.

Mitcheson, P. D., E. M. Yeatman, G. K. Rao, A. S. Holmes, and T. C. Green (2008). Energy harvesting from human and machine motion for wireless electronic devices. *Proceedings of the IEEE 96*(9), 1457–1486.

Miyagawa, H., C. Sato, T. Mase, E. Drown, L. T. Drzal, and K. Ikegami (2005). Transverse elastic modulus of carbon fibers measured by raman spectroscopy. *Materials Science and Engineering: A 412*(1-2), 88–92.

Moon, C. K., J.-O. Lee, H. H. Cho, and K. S. Kim (1992). Effect of diameter and surface treatment of fiber on interfacial shear strength in glass fiber/epoxy and hdpe. *Journal of applied polymer science 45*(3), 443–450.

Mu, J., C. Hou, G. Wang, X. Wang, Q. Zhang, Y. Li, H. Wang, and M. Zhu (2016). An elastic transparent conductor based on hierarchically wrinkled reduced graphene oxide for artificial muscles and sensors. *Advanced Materials 28*(43), 9491–9497.

Nakagawa, H., Y. Hara, S. Maeda, and S. Hasimoto (2011). A pendulum-like motion of nanofiber gel actuator synchronized with external periodic ph oscillation. *Polymers 3*(1), 405–412.

Ngah, S. A. and A. C. Taylor (2016). Toughening performance of glass fibre composites with core–shell rubber and silica nanoparticle modified matrices. *Composites Part A: Applied Science and Manufacturing 80*, 292–303.

Nofar, M., S. Hoa, and M. Pugh (2009). Failure detection and monitoring in polymer matrix composites subjected to static and dynamic loads using carbon nanotube networks. *Composites Science and Technology 69*(10), 1599–1606.

Novozhilov, V. V. (1999). *Foundations of the nonlinear theory of elasticity.* Courier Corporation.

Okazaki, J., Y. Osaki, H. Hosaka, K. Sasaki, H. Yamakawa, and K. Itao (2002). Dynamic analysis and impedance control of automatic power generators using mechanical vibration. *Tech. Dig*, 110–113.

Ottman, G. K., H. F. Hofmann, A. C. Bhatt, and G. A. Lesieutre (2002). Adaptive piezoelectric energy harvesting circuit for wireless remote power supply. *IEEE Transactions on power electronics 17*(5), 669–676.

Ottman, G. K., H. F. Hofmann, and G. A. Lesieutre (2003). Optimized piezoelectric energy harvesting circuit using step-down converter in discontinuous conduction mode. *IEEE Transactions on power electronics 18*(2), 696–703.

Özden Yenigün, E., Y. Z. Menceloğlu, and M. Papila (2012). Mwcnts/p (st-co-gma) composite nanofibers of engineered interface chemistry for epoxy matrix nanocomposites. *ACS applied materials & interfaces 4*(2), 777–784.

Paracha, A. M., P. Basset, P. Lim, F. Marty, and T. Bourouina (2006). A bulk silicon-based vibration-to-electric energy converter using an in-plane overlap plate (ipop) mechanism. In *PowerMEMS2006 Workshop Proceedings*.

Parnes, R. and A. Chiskis (2002). Buckling of nano-fibre reinforced composites: a reexamination of elastic buckling. *Journal of the Mechanics and Physics of Solids 50*(4), 855–879.

Patel, J. S., V. M. Boddu, M. W. Brenner, and A. Kumar (2016). Effect of fabric structure and polymer matrix on flexural strength, interlaminar shear stress, and energy dissipation of glass fiber-reinforced polymer composites. *Textile Research Journal 86*(2), 127–137.

Pimenta, S. and S. T. Pinho (2011). Recycling carbon fibre reinforced polymers for structural applications: technology review and market outlook. *Waste management 31*(2), 378–392.

Puttock, M. and E. Thwaite (1969). *Elastic compression of spheres and cylinders at point and line contact*. Commonwealth Scientific and Industrial Research Organization Melbourne, Australia.

Qian, H., A. Bismarck, E. S. Greenhalgh, and M. S. Shaffer (2010a). Carbon nanotube grafted carbon fibres: a study of wetting and fibre fragmentation. *Composites Part A: Applied science and manufacturing 41*(9), 1107–1114.

Qian, H., A. Bismarck, E. S. Greenhalgh, and M. S. Shaffer (2010b). Carbon nanotube grafted silica fibres: Characterising the interface at the single fibre level. *Composites Science and Technology 70*(2), 393–399.

Rao, S. S. and F. F. Yap (2011). *Mechanical vibrations*, Volume 4. Prentice Hall Upper Saddle River.

Rosen, B. W. (1965). Mechanics of composite strengthening.

Roy, S., F. Hussain, K. Narasimhan, K. Vengadassalam, and H. Lu (2007). E-glass/polypropylene pultruded nanocomposite: Manufacture, characterisation, thermal and mechanical properties. *Polymers & polymer composites 15*(2), 91.

Roy, S., H. Lu, K. Narasimhan, and F. Hussain (2005). Characterization and modeling of strength enhancement mechanisms in a polymer/clay nanocomposite. In *46th AIAA/ASME/ASCE/AHS/ASC Structures, Structural Dynamics and Materials Conference*, pp. 1853.

Safaei, M., A. Sheidaei, M. Baniassadi, S. Ahzi, M. M. Mashhadi, and F. Pourboghrat (2015). An interfacial debonding-induced damage model for graphite nanoplatelet polymer composites. *Computational Materials Science 96*, 191–199.

Sager, R., P. Klein, D. Lagoudas, Q. Zhang, J. Liu, L. Dai, and J. Baur (2009). Effect of carbon nanotubes on the interfacial shear strength of t650 carbon fiber in an epoxy matrix. *Composites Science and Technology 69*(7-8), 898–904.

Schultheisz, C. R. and A. M. Waas (1996). Compressive failure of composites, part i: testing and micromechanical theories. *Progress in Aerospace Sciences 32*(1), 1–42.

Sellinger, A. T., D. H. Wang, L.-S. Tan, and R. A. Vaia (2010). Electrothermal polymer nanocomposite actuators. *Advanced Materials 22*(31), 3430–3435.

Sharma, S. and S. Lakkad (2011). Effect of cnts growth on carbon fibers on the tensile strength of cnts grown carbon fiber-reinforced polymer matrix composites. *Composites Part A: Applied Science and Manufacturing 42*(1), 8–15.

Shigley, J. E. (2011). *Shigley's mechanical engineering design.* Tata McGraw-Hill Education.

Sneller, A. J. and B. P. Mann (2010). On the nonlinear electromagnetic coupling between a coil and an oscillating magnet. *Journal of Physics D: Applied Physics 43*(29), 295005.

Soutis, C. (2005). Carbon fiber reinforced plastics in aircraft construction. *Materials Science and Engineering: A 412*(1-2), 171–176.

Steif, P. S. (1987). An exact two-dimensional approach to fiber micro-buckling. *International journal of solids and structures 23*(9), 1235–1246.

Su, Y., B. Ji, K.-C. Hwang, and Y. Huang (2012). Micro-buckling in the nanocomposite structure of biological materials. *Journal of the Mechanics and Physics of Solids 60*(10), 1771–1790.

Sui, X. and H. D. Wagner (2009). Tough nanocomposites: the role of carbon nanotube type. *Nano letters 9*(4), 1423–1426.

Swadener, J., K. Liechti, and A. De Lozanne (1999). The intrinsic toughness and adhesion mechanisms of a glass/epoxy interface. *Journal of the Mechanics and Physics of Solids 47*(2), 223–258.

Swolfs, Y., R. M. McMeeking, I. Verpoest, and L. Gorbatikh (2015). Matrix cracks around fibre breaks and their effect on stress redistribution and failure development in unidirectional composites. *Composites Science and Technology 108*, 16–22.

Tadjbakhsh, I. G. and Y. Wang (1992). Fiber buckling in three-dimensional periodic-array composites. *International journal of solids and structures 29*(24), 3169–3183.

Tahhan, M., V.-T. Truong, G. M. Spinks, and G. G. Wallace (2003). Carbon nanotube and polyaniline composite actuators. *Smart materials and structures 12*(4), 626.

Talreja, R. (2016). Matrix and fiber–matrix interface cracking in composite materials. In *Modeling Damage, Fatigue and Failure of Composite Materials*, pp. 87–96. Elsevier.

Tang, L.-G. and J. L. Kardos (1997). A review of methods for improving the interfacial adhesion between carbon fiber and polymer matrix. *Polymer composites 18*(1), 100–113.

Thostenson, E., W. Li, D. Wang, Z. Ren, and T. Chou (2002). Carbon nanotube/carbon fiber hybrid multiscale composites. *Journal of Applied physics 91*(9), 6034–6037.

Tseng, C.-H., C.-C. Wang, and C.-Y. Chen (2007). Functionalizing carbon nanotubes by plasma modification for the preparation of covalent-integrated epoxy composites. *Chemistry of Materials 19*(2), 308–315.

Tsotsis, T. K. (2009). Interlayer toughening of composite materials. *Polymer composites 30*(1), 70–86.

Tsuda, T., T. Ogasawara, S.-Y. Moon, K. Nakamoto, N. Takeda, Y. Shimamura, and Y. Inoue (2014). Three dimensional orientation angle distribution counting and calculation for the mechanical properties of aligned carbon nanotube/epoxy composites. *Composites Part A: Applied Science and Manufacturing 65*, 1–9.

Tutuncuoglu, K. and A. Yener (2012). Optimum transmission policies for battery limited energy harvesting nodes. *IEEE Transactions on Wireless Communications 11*(3), 1180–1189.

Ulaby, F. T., U. Ravaioli, and E. Michielssen (2014). *Fundamentals of applied electromagnetics*. Prentice Hall.

Upadhyaya, P., S. Roy, M. H. Haque, and H. Lu (2013). Influence of nano-clay compounding on thermo-oxidative stability and mechanical properties of a thermoset polymer system. *Composites Science and Technology 84*, 8–14.

Waas, A. (1992). Effect of interphase on compressive strength of unidirectional composites. *ASME Transactions Series E Journal of Applied Mechanics 59*, S183–S188.

Waas, A., C. Babcock, and W. Knauss (1990). A mechanical model for elastic fiber microbuckling. *Journal of Applied Mechanics 57*(1), 138–149.

Waas, A. M. and C. R. Schultheisz (1996). Compressive failure of composites, part ii: experimental studies. *Progress in Aerospace Sciences 32*(1), 43–78.

Williams, C., C. Shearwood, M. Harradine, P. Mellor, T. Birch, and R. Yates (2001). Development of an electromagnetic micro-generator. *IEE Proceedings-Circuits, Devices and Systems 148*(6), 337–342.

Williams, C. and R. B. Yates (1996). Analysis of a micro-electric generator for microsystems. *sensors and actuators A: Physical 52*(1-3), 8–11.

Williams, J. C. and E. A. Starke Jr (2003). Progress in structural materials for aerospace systems1. *Acta Materialia 51*(19), 5775–5799.

Wittrick, W. H. (1966). On elastic wave propagation in helical springs. *International Journal of Mechanical Sciences 8*(1), 25–47.

Xu, T. (2017). *Characterization and modeling of mechanical behavior of polymers and composites at small scales by nanoindentation*. PhD dissertaiton, The University of Texas at Dallas.

Xu, Y. L. and K. L. Reifsnider (1993). Micromechanical modeling of composite compressive strength. *Journal of Composite Materials 27*(6), 572–588.

Xu, Z., L. Chen, Y. Huang, J. Li, X. Wu, X. Li, and Y. Jiao (2008). Wettability of carbon fibers modified by acrylic acid and interface properties of carbon fiber/epoxy. *European polymer journal 44*(2), 494–503.

Yang, Q. and G. Li (2016). A top-down multi-scale modeling for actuation response of polymeric artificial muscles. *Journal of the Mechanics and Physics of Solids 92*, 237–259.

Yeh, J. and J. Teply (1988). Compressive response of kevlar/epoxy composites. *Journal of composite materials 22*(3), 245–257.

Yeo-Heung, Y., A. Miskin, P. Kang, S. Jain, S. Narasimhadevara, D. Hurd, V. Shinde, M. J. Schulz, V. Shanov, P. He, et al. (2006a). Carbon nanofiber hybrid actuators: Part i-liquid electrolyte-based. *Journal of intelligent material systems and structures 17*(2), 107–116.

Yeo-Heung, Y., A. Miskin, P. Kang, S. Jain, S. Narasimhadevara, D. Hurd, V. Shinde, M. J. Schulz, V. Shanov, P. He, et al. (2006b). Carbon nanofiber hybrid actuators: Part ii-solid electrolyte-based. *Journal of intelligent material systems and structures 17*(3), 191–197.

Yongbo, Z. and F. Huimin (2011). On the longitudinal compressive strength prediction of unidirectional laminated composites based on an improved model. *Polymer Composites 32*(11), 1817–1826.

Yun, Y.-H., V. Shanov, M. J. Schulz, S. Narasimhadevara, S. Subramaniam, D. Hurd, and F. Boerio (2005). Development of novel single-wall carbon nanotube–epoxy composite ply actuators. *Smart materials and structures 14*(6), 1526.

Zeng, Y., L. Ci, B. J. Carey, R. Vajtai, and P. M. Ajayan (2010). Design and reinforcement: vertically aligned carbon nanotube-based sandwich composites. *ACS nano 4*(11), 6798–6804.

Zhang, F.-H., R.-G. Wang, X.-D. He, C. Wang, and L.-N. Ren (2009a). Interfacial shearing strength and reinforcing mechanisms of an epoxy composite reinforced using a carbon nanotube/carbon fiber hybrid. *Journal of materials science 44*(13), 3574–3577.

Zhang, G. and R. A. Latour Jr (1994). An analytical and numerical study of fiber microbuckling. *Composites science and technology 51*(1), 95–109.

Zhang, S., N. Zhang, C. Huang, K. Ren, and Q. Zhang (2005). Microstructure and electromechanical properties of carbon nanotube/poly (vinylidene fluoridetrifluoroethylenechlorofluoroethylene) composites. *Advanced Materials 17*(15), 1897–1901.

Zhao, F. and Y. Huang (2010). Improved interfacial properties of carbon fiber/epoxy composites through grafting polyhedral oligomeric silsesquioxane on carbon fiber surface. *Materials Letters 64*(24), 2742–2744.

Zhu, J., J. Kim, H. Peng, J. L. Margrave, V. N. Khabashesku, and E. V. Barrera (2003). Improving the dispersion and integration of single-walled carbon nanotubes in epoxy composites through functionalization. *Nano letters 3*(8), 1107–1113.

Zhu, Y., C. E. Bakis, and J. H. Adair (2012). Effects of carbon nanofiller functionalization and distribution on interlaminar fracture toughness of multi-scale reinforced polymer composites. *Carbon 50*(3), 1316–1331.

Zu, M., Q. Li, Y. Zhu, M. Dey, G. Wang, W. Lu, J. M. Deitzel, J. W. Gillespie Jr, J.-H. Byun, and T.-W. Chou (2012). The effective interfacial shear strength of carbon nanotube fibers in an epoxy matrix characterized by a microdroplet test. *Carbon 50*(3), 1271–1279.

BIOGRAPHICAL SKETCH

Xuemin Wang is a doctoral candidate in the department of Mechanical Engineering at The University of Texas at Dallas. Her research interests focus on experimental mechanics, mechanics of time dependent materials, finite element analysis and theoretical analysis of multi-physics coupling mechanisms. She received her master's degree in computation mathematics at Xi'an Jiaotong University, and bachelor's degree in Mathematics at Shaanxi Normal University. She received the Louis Beecherl, Jr. Graduate Fellowship twice.

CURRICULUM VITAE

Xuemin Wang

May 31, 2018

Contact Information:

Department of Mechanical Engineering
The University of Texas at Dallas
800 W. Campbell Rd.
Richardson, TX 75080-3021, U.S.A.

Email: xxw140030@utdallas.edu

Educational History:

B.S., Mathematics and Information Science, Shaanxi Normal University, 2006
M.S., Computational Mathematics, Xi'an Jiaotong University, 2013
Ph.D., Mechanical Engineering, The University of Texas at Dallas, 2018

Mechanical Characterization and Modeling of Material Performance during Compression and Actuation
Ph.D. Dissertation
Mechanical Engineering Department, The University of Texas at Dallas
Advisors: Dr. Hongbing Lu

Employment History:

Teaching and Research Assistant, The University of Texas at Dallas, January 2014 – August 2018

Professional Recognitions and Honors:

The Louis Beecherl, Jr. Graduate Fellowship, The University of Texas at Dallas, 2015
Phi Kappa Phi Honor Society, The University of Texas at Dallas, 2016
The Louis Beecherl, Jr. Graduate Fellowship, The University of Texas at Dallas, 2017

Professional Memberships:

The American Society of Mechanical Engineers (ASME), 2017 – 2018